Chapter 1

Introduction

In recent years, the remarkable advances in medical imaging instruments have increased their use considerably for diagnostics as well as planning and follow-up of treatment. The concepts and techniques in medical image processing used to analyze and manipulate medical images after they have been generated or digitized.

Medical imaging is the process by which physicians evaluate an area of the subject's body that is not normally visible. Medical imaging may be "clinical", seeking to diagnose and examine disease in specific human patients. Alternatively, it may be research-motivated, attempting to understand processes in humans or animal models. Many of the techniques developed for medical imaging also have scientific and industrial applications.

In this thesis, medical image processing is used to identify the shape and the location of optic disk (OD) which is the brightest object in the healthy retinal image for helping medical doctor to diagnose the retinopathy of prematurity (ROP) disease and prevent the patient from blindness.

The developing of application software in digital image processing will help the clinicians to analyze the area surrounding the optic nerve which is predictive of the level of ROP. With the wide range and type of retinal images present a specific type of problem in the analysis of optic disk; many techniques have been purposed including detection of the OD regions by clustering the brightest pixels in retinal image and locating potential OD area. Other techniques have been recently proposed, based on a model of vascular structure by Foracchia *et al*. (2004). They use a geometrical parametric model locating at the center point of OD. Akita and Kuga (1982), trace the parent-child relationship between blood vessels segments, tracking back to the center of the optic disk. Lalonde *et al*. (2001) used pyramidal decomposition and Hausdorff-based template matching that is guided by scale tracking of large objects using multi-resolution image decomposition. This method is effective, but rather complex. In three dimensional reconstructions of conventional stereo optic disk image procedures, Kong *et al*. (2004) presented the resulting 3 dimensional contour images that show optic disk structure clearly and intuitively, helping physicians in understanding the stereo disk photograph. Cox and Wood (1991) presented a semi-automated method to indicate external points on the boundary which were automatically connected by tracing along the boundary. Morris and Cox (1993) initially presented a completely automatic method which traced between points on the boundary identified automatically by their grey level gradient properties. Sinthanayothin *et al*. (1999) used the rapid intensity variation between the dark vessels and the bright nerve fibers to locate the optic disk. However, they found that this algorithm often failed for fundus images with a large number of white lesions. Lee (1991) also applied an active contour model to high resolution images centered on the optic nerve head and his problem caused by the boundary of the pallor and by very faint or missing edges. Huiqi *et al*. (2001) used PCA and ASM technique to apply in detecting the optic disk centre and approximate the optic disk area by using “disk space” but this algorithm failed in unclear shape of optic disk. Kavitha (2005) used morphological operations and multilevel thresholding to extract the brighter regions that includes optic disk and exudates. Jelinek *et al.* (2005) used Canny edge detection, template matching and Haar transform to detect optic disk boundary. The most effective method, active contour model or snake, was used to detect the optic disk by Osareh *et al.* (2002), Mendels *et al.* (1999), Chanwimaluang and Fan (2003). Corona *et al.* (2002) used an algorithm, combining power cepstrum and zero-mean-normalized cross correlation techniques, which extract depth information using coarse-to-fine disparity between corresponding windows in a stereo pair. The gray level encoded sparse disparity matrix is subjected to a cubic B-spline operation to generate smooth representations of optic disk surface and new three-dimensional (3-D) matrics from isodisparity contours. Niemeijer *et al.* (2007) used a novel method that determines whether a macula centered retinal image is from the left or right eye and automatically detects the optic disk, the fovea and the vascular arch by inferring the location of a set of landmarks placed on these structures. Tobin *et al.* (2006) presented results for the automatic detection of the optic nerve using digital red-free fundus photography. The location of the optic disk is predicted by using a two-class, Bayesian classifier. Chrastek *et al.* (2004) presented methods for automated segmentation of the optic disk in the two imaging modalities, namely in images of scanning laser tomography in color image. These methods developed for each modality separately which link in the registration of two imaging modalities containing partly complementary information.

However, most of techniques mentioned above have been mainly focused on adult retinal images where the retina is well developed. In this thesis, we present the algorithms that automatically detect optic disk in retinopathy of prematurity(ROP), a disease cause of blindness in the infant. If appropriate treatment is given in the early stages of blindness can be prevented. The algorithm is evaluated against ROP infant database from Kingston University, UK, and Thammasat University, Thailand compared with ground truth image marked by ophthalmologist.

1.1 Motivation

The coming generation of babies, blinded with ROP, may not forgive the attitude that many ophthalmologists adopt to avoid the painstaking effort of ROP screening. The financial, social and emotional crisis of having a blind child cannot be avoided without a committed team effort, particularly by the ophthalmologist and the neonatologist from the very beginning of life. Optic disk segmentation is a necessary step in this structured analysis of ROP because the location of optic disk is essential in retinal image analysis to measure distance and identify other anatomical parts in retinal images. Pathology on or near the optic disk can have a more severe effect in vision. In the previous, identification of the optic disk from infant's retinal image was difficult due to several factors. The disk may be located in the different positions and low-contrast in the retinal image. Once the optic disk region was found, the intersecting blood vessels that converge in the middle of the disk created a heterogeneous section then the identification of OD was determined only by an expert human. That is a time-consuming, highly skilled task, susceptible to subjective variation and error. There is consequently a pressing need for reliable automated analysis of digitized fundus images. Later, most of techniques in optic disk detection were implemented but it worked pretty well in adult retinal image, a few techniques was used for infant's retinal image. Then this thesis provides purposed methods to help ophthalmologist in ROP screening that will reduce cost and time and prevent the children from losing of vision.

1.2 Objectives

According to the motivation, this research aims at the following objectives.

1. To detect the variable appearance of ODs in ROP infant's retinal images (intensity, color, contour definition, macula-centered and OD-centered images).
2. To present the purposed methods in locating the optic disk in low-contrast infant's retinal image
3. To help a medical doctor to evaluate the ROP disease in the earlier stage, that will help the childhood not lose their vision.
4. Have an efficiency and reliable result to identify and extract the optic disk.

1.3 Overview

This thesis contains six chapters. Chapter 1 gives an introduction of the research. It presents a survey on detecting the optic disk. The survey also focuses infant's retinal image. In addition, motivation, research objective and overview of thesis are included in this chapter. In Chapter 2, the background related to techniques, the characteristics of optic disk, ROP, system, materials and medical importance of optic disk detection are presented. Chapter 3 describes our purposed algorithm in Automatic Detection of Optic Disk from Fundus Images of ROP Infant Using 2D Circular Hough Transform. In this chapter, the method to detect the optic disk by using Circular Hough Transform, experimental verification, experimental results, conclusion and discussion are included. Chapter 4, the technique in Automatic Optic Disk Detection from Low Contrast Retinal Images of ROP Infant Using GVF Snake is presented. In this chapter, the method to extract optic disk by using PCA and GVF Snake, the framework, experimental verification, experimental results, conclusion and discussions are included. Chapter 5, Automatic Optic Disk Detection from Low Contrast Retinal Images of ROP Infant Using Mathematical Morphology is included, the method of mathematical morphology, experimental verification, experimental results, conclusion and discussion are purposed. A conclusion is given in the last chapter, Chapter 6, the last chapter includes the summary and the key contributions of the research. The recommendations for future study are also given.

Chapter 2

Background

This chapter presents some background, which is related to optic disk detection. The topics include characteristics of optic disk, retinopathy of prematurity(ROP), system and materials and medical importance of optic disk detection.

2.1 Optic disk characteristic

The optic disk, shown in Figure 2.1(a), is also called the blind spot. It is called this because there are no receptors in the part of the retina. The optic disk is the brightest part in the normal fundus image that can be seen as a pale, round or oval disk in shape. It is the entrance region of blood vessels and optic nerves to the retina and it often works as a landmark and reference for the other features in the retinal fundus image. Usually in a normal eye, physical diameter of the optic disk is about 1.5 mm to 1.7 mm on average. The location of the optic disk is essential in retinal image analysis to measure distance and identify other anatomical parts in retinal images. Pathology on or near the optic disk can have a more severe effect in vision.

2.1.1 Understanding the optic disk

Colour: Red-yellow; the yellowish color (optic cup)
Form and size: Round to oval with diameter ranging from 1.5 mm to 1.7 mm
Margins: Sharply outline.
Vessels: They originate within the perimeter of the disk and both the arteries and veins appear distinct.

2.2 Retinopathy of Prematurity (ROP)

Retinopathy of Prematurity (ROP) is a developmental disease used to describe abnormal blood vessels and scar tissue growing inside and over the retina of the eye. The incidence of ROP rises with lower gestational age and birth weight. In patients with ROP, the premature baby's blood vessels in his eye are very sensitive to oxygen and light then the blood vessels stop growing and new abnormal blood vessels grow instead of normal retinal blood vessels. It usually affects babies and leads to blindness or poor vision (McNamara and Connolly, 1999; Palmer *et al*., 1991).

The location of ROP, shown in Figure 2.1(b), refers to the location relative to the optic nerve. The retinal vessels normally start their growth at the optic nerve and gradually move toward the edge of the retina. Vessels that are farther from the optic nerve or closer to the edge of the retina are more mature and less concerning. The ophthalmologist can be examined the ROP symptoms at four weeks of baby's age. The following information presents pathogenesis, cause and risk factor, staging disease and classification of ROP.

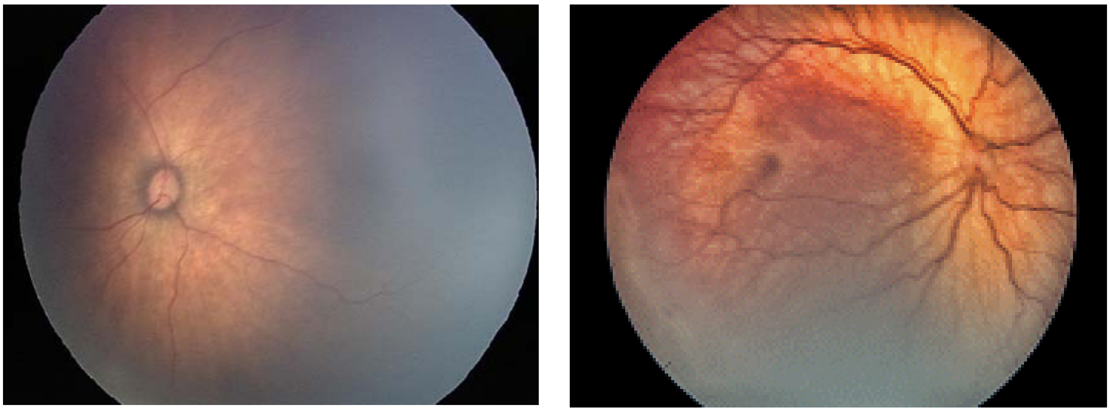

(a) (b)

Figure 2.1 (a) Optic Disk Image (b)Optic Disk with the condition ROP

2.2.1 Pathogenesis

1. At twelve to eighteen weeks of gestation, vascularization of the retina begins.
2. First the primitive future endothelial cells form cords that canalize into a network of evenly spaced capillaries, which further differentiate into primitive and then mature arterioles and venules.
3. Vessels grow outward from the optic disk toward the nasal and temporal periphery of the retina.
4. If an adverse event (see Causes and Risk Factors) occurs to these vessels, the natural progress is arrested.
5. After the initial injury, vessel growth can resume normally or the primitive vessels pile up within the retina, growing without forward progress and forming a ridge of tissue that can become extremely large. This tissue may then regress, and vessels once again progress toward the periphery, or the ROP can worsen through the growth of fibrovascular tissue into the vitreous cavity.
6. The formation of scar tissue and its progression over the retina and into the vitreous body may determine the prognosis and visual outcome.
7. In severe cases these abnormal vessels may grow into the vitreous cavity and cause tractionalretinal detachment and subsequent blindness.
8. The human retina may not be completely vascularized at term. This may account for the rare occurrence of ROP in full term neonates.

2.2.2 Causes and risk factors

The exact causes of ROP are not completely understood. The degree of prematurity and birth weight of a baby play a big part in the development of ROP. The small and sick baby has a high risk to be ROP. The premature baby's blood vessels in his eye are very sensitive to oxygen and light. It usually affects babies less than 1500 grams. There are a number of risk factors for the development of ROP (McNamara and Connolly, 1999).

1. **Birth weight and gestational age:** These are the two most important risk factors for ROP. The younger the gestational age and lesser the birth weight, the greater are the chances of developing ROP. More premature neonates are likely to develop a more severe from of disease.

2. **Oxygen therapy:** Though not the only aetiological agent, as it was once thought to be,

excessive use is an important contributory factor. It has been seen that premature neonates develop ROP even without being exposed to oxygen and, conversely, others do not develop ROP despite being on oxygen.

3. **Other factors:** A number of other risk factors in the development of ROP include sepsis, multiple blood transfusions, multiple births, hyaline membrane disease, using of aminophylline, antibiotics, apnoeic spells, low pH, and ultraviolet light therapy

2.2.3 Staging of disease

The definition in staging of disease is described below:
Stage 1: Demarcation line
This is a flat white line within the plane of the retina that clearly delineates the vascularized posterior retina from the vascular anterior portion. Abnormal branching or arcading of vessels is recognizable immediately posterior to the demarcation line (Figure 2.2(a)).

Stage 2: Ridge of the demarcation line
A ridge(R) of scar tissue and new blood vessels place in the demarcation line. The white line now has width and height and occupies some volume. Vascular shunting occurs in this stage (Figure 2.2(b)).

Stage 3: Ridge with extra-retinal fibrovascular proliferation
In this step, the vascular ridge was increased the size with growth of fibrovascular tissue on the ridge and extending out into the vitreous (Figure 2.2(c)).

Stage 4: Subtotal (Partial) Retinal Detachment
a. Stage 4A: Macula on - detachment does not include the macula, and the vision may be good.
b. Stage 4B: Macula off - macula is detached, and the visual potential is markedly decreased.

Stage 5: Complete retinal detachment

Stage 6: Plus Disease: Vessels are dilated and tortuous.
It may also include growth and dilation of abnormal blood vessels on the surface of the iris, rigidity of the iris and vitreous haze (exudates along the retinal vessels).

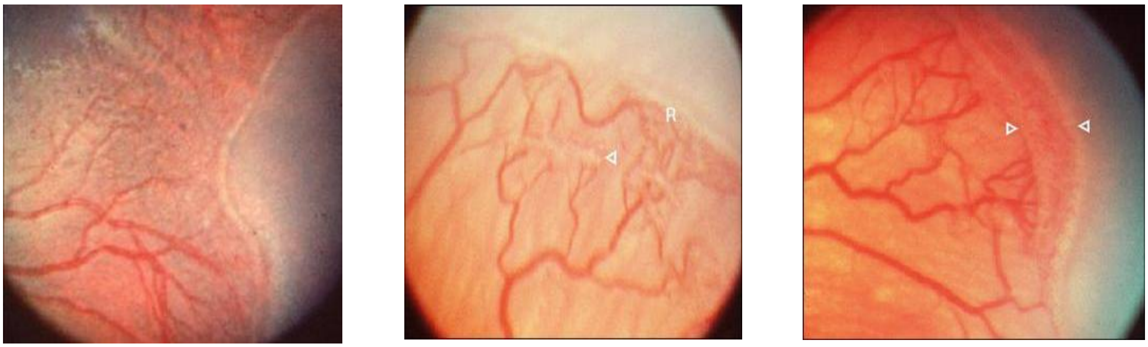

(a) **(b)** **(c)**

Figure 2.2 (a) Demarcation line (b) Ridge of the demarcation line (c) Ridge with extra-retinal fibrovascular proliferation

2.2.4 Classification of ROP:

The International Classification System of ROP allows the examiner to specify parameters of the disease, location, extent of developing vasculature involved and staging.

Location: is expressed as zone I, II, or III, each zone is centered on the optic disk because normal retinal vascular growth progresses peripherally from the disk toward the ora serrata (Figure 2.3).
1. Zone I: Posterior pole or inner zone; in all directions from the optic disk to a distance twice that between the disk and the macula.
2. Zone II: From the edge of zone I peripherally to a point tangential to the nasal ora serrata and an area near the temporal anatomic equator.
3. Zone III: The remaining crescent of the fundus temporally anterior to zone II. This zone is the last to be vascularized.

Table 2.1: Area of ROP Involvement Zones

Zone I	A circle is drawn on the posterior pole, with the optic disk as the centre and twice the disk-macula distance as the radius, constitutes zone I. Any ROP in this zone is usually very severe because of a large peripheral area of avascular retina
Zone II	A circle is drawn with the optic disk as the centre and disk to nasal ora serrata as the radius. The area between zone I and this boundary constitutes zone II
Zone III	The temporal arc of retina left beyond the radius of zone II is zone III (Figure 2.3)
Extent	The extent is denoted by the clock hours of retinal involvement in the particular zone
Rush Disease	This is rapidly progressive ROP in zone I, usually seen in extremely sick babies

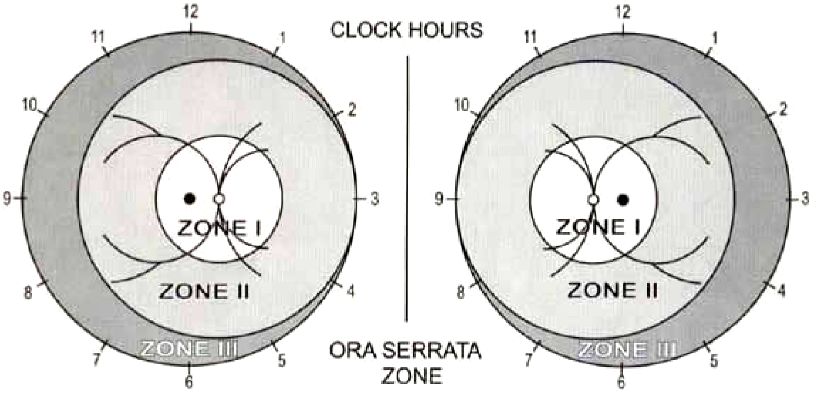

Figure 2.3 Guideline diagram used in the classification of retinopathy of prematurity

2.3 System and Materials

In this work, the system implemented in MATLAB 7.0.4(R14) on a 3 GHz Pentium 4 machine, the images obtained from Kingston University, UK and Thammasat hospital, Thailand. The example of retinal images in ROP Infant was shown in Figure 2.4. There were a representative sample of a set of normal retinal image and abnormalities. The training set was randomly from the screening set of one hundred retinal images. The image size was set to 640 x 480 pixels, 72 inch/pixel. All the images were JPEG compressed. In order to acquire the pathological test set, all cases of optic disk detection marked as ground truth image by the ophthalmologists.

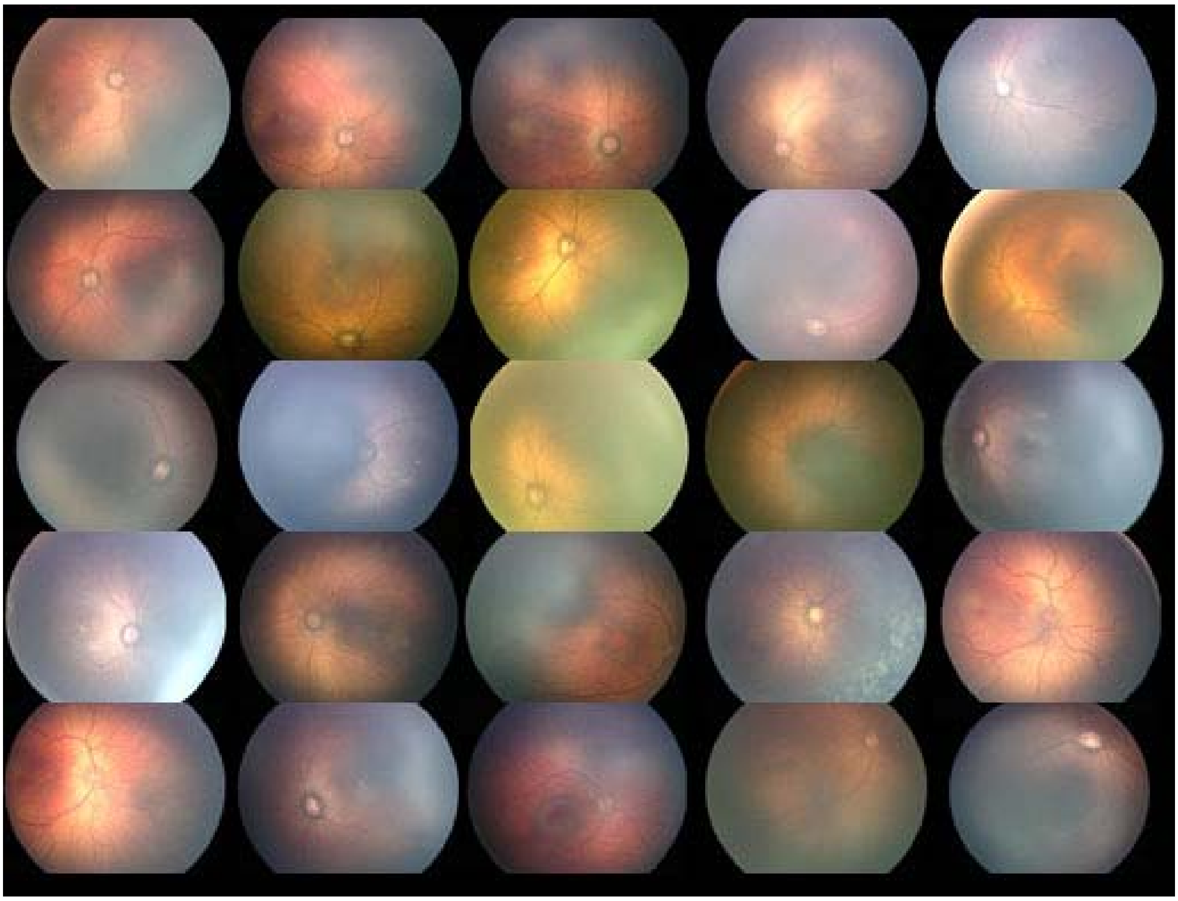

Figure 2.4 The example of optic disk data set

2.4 Medical Importance of Optic Disk Detection

Precise localization of optic disk boundary is an important sub problem of higher level problems in ophthalmic image processing. Specifically, in retinopathy of prematurity, proliferative diabetic retinopathy, fragile vessels develop in the retina and largely in the OD region, in response to circulation problems created during earlier stages of the disease. If the optic disk has been identified, the position of areas of clinical importance such as the fovea may be determined. Moreover, OD detection is fundamental for establishing a frame of reference within the retinal image and is, thus, important for any image analysis application. Current methods of detection and assessment in the stage of ROP are manual, expensive, potentially inconsistent, and require highly trained personnel to facilitate the process by searching large numbers of fundus images. Many of these images from screening programmes will be normal, but some will require grading of abnormalities by ophthalmologist. When abnormalities do not treatment immediately, the patient may loss the vision. In contrast to this, a good, automatic method based on modern digital image processing technique will be faster, will need less may be no human intervention, and will yield consistent results.

Chapter 3

Automatic Detection of Optic disk from Fundus Images of ROP Infant Using 2D Circular Hough Transform

In this chapter, a method of automatic detection of an Optic Disk in low-contrast infant's digital fundus images based on circular Hough transform is proposed. Number of dimensions of normal circular Hough Transforms histogram is reduced from 3 to 2 dimensions based on an approximation of OD radius. First few circles are approximated by using maximum points from Hough space. A circle with the best fit to OD edge image is chosen. The results are validated with ophthalmologists' hand-drawn ground truth. The overview of Circular Hough Transform, methodology, experimental verification, experimental results, conclusion and discussion are included in this chapter.

3.1 Overview of Circular Hough Transform

The Hough transform is a technique to identify the locations and orientations of certain types of features in a digital image. The transform consists of parameterized description of a feature at any given location in the original image space. A multi-dimensional array in the space defined by these parameters is then generated. At each point, a value is accumulated, indicating probability of an object generated by the parameters defined at that point fits the given image. Any points in the array that have relatively higher values are used to describe features that may be projected back onto the image. The higher to value, the bigger possibility that the features actually present in the image (Gonzalez, 2002).

In essence the Hough Transform produces a set of parameters which describe a boundary curve of the expected type that represents the best fit to the set of edge points in the given image. This is done by transforming every edge position in the image 'space' (as defined by x and y axes) into a corresponding curve within a 'parameter space', or 'Hough space'. A point in the Hough space where many curves intersect represents a simultaneous solution to the parametric equation for all of the edges in the image space whose coordinates gave rise to those curves. This indicates a strong likelihood of a boundary shape of the expected type having been detected in the image space. The coordinates of the point of the intersection in the Hough space correspond to the parameters of the curve detected in the image space; the greater the number of intersections, the greater the confidence that the detected boundary shape is genuine. It is this 'voting' effect that gives the Hough Transform its characteristic immunity to noise and discontinuous boundaries.

For example, consider the case where a straight line is to be detected. A point, (x_i, y_i), in input space presumed to lie on this line (conventionally defined by the standard linear equation, $y = mx + c$) produces a locus of points in parameters space for all possible lines upon which it could lie (thus defined as $c = -mx + y$), as shown in Figure 3.1. A second point in input space, (x_j, y_j), similarly produces a locus of points in Hough space. Thus when all points of interest in input space (previously detected edges) have been transformed to loci in Hough space, the intersections of these loci give a vote as to the best set of parameters for the unique line in the input space which will join all given points. The position of maximum intersection yields the parameters m_b for the best fit solution.

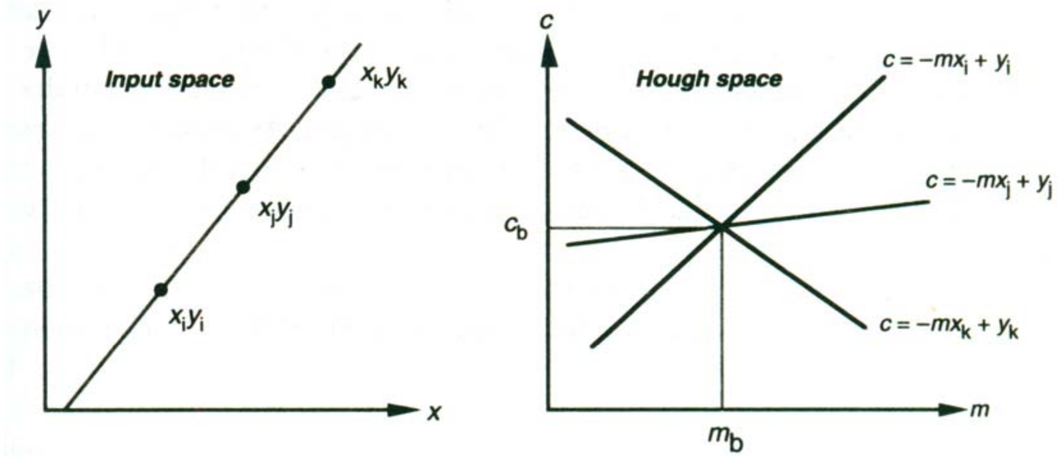

Figure 3.1. The Hough Transform used for straight line detection

One problem with this approach is that when implemented in discrete digital form a very large array of Hough space 'accumulators' is required to store all possible votes since the range of values should extend from minus infinity to infinity (e.g. a perfectly vertical line in input space has an infinite gradient). One way to overcome this limitation is to utilize polar coordinates length, r, and angle, ø, of normal vector connecting it to the origin (see Figure 3.2). These parameters are related to the x and y coordinates by the expression

$$r = x\cos\phi + y\sin\phi \qquad (3.1)$$

The three points shown in the input image are mapped into the Hough space (now in (r,ϕ) form). Each point in the input image, a, b or c, transforms to a sinusoidal curve which is plotted over the range 0 to 2π radians. The position of maximum intersection can again be found and these unique values of r_b and ϕ_b used to define the best straight line detected in the input image which joins the given pixel points, of edges. As expected all the curves exhibit a symmetrical positive and negative response. Therefore the amount of computation can be halved by plotting curves in the Hough space only over the range 0 to π radians (Awcock and Thomas, 1996).

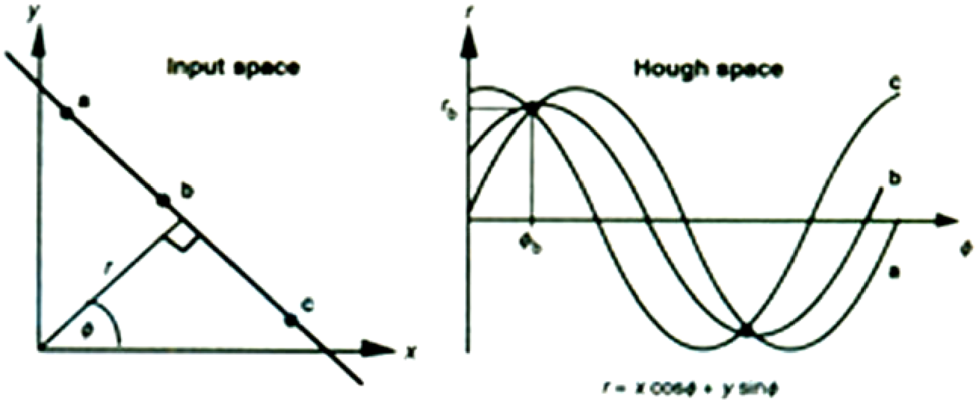

Figure 3.2. The Hough Transform-polar representation

In Figure 3.3, the Hough transform can be used for representing objects that can be parameterized mathematically. For example, in our case, a circle can be parameterized by an Equation. (3.2).

$$(x-a)^2+(y-b)^2=r^2 \qquad (3.2)$$

where *(a,b)* is the coordinate of the center of the circle that passes through *(x,y)* and *r* is its radius. From this equation, it can be seen that three parameters are used to formalize a circle which means that Hough space will be a three-dimensional space for this case.

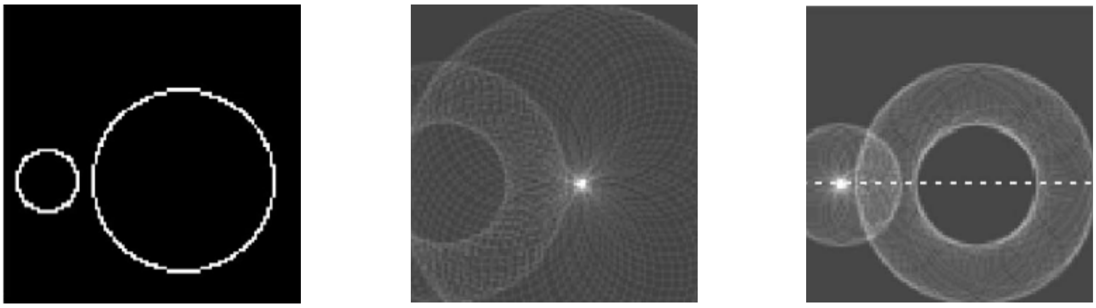
(a) (b) (c)

Figure 3.3 a) Binary dataset consisting two circles of radii 10 and 30 units b) result of using circular Hough Transform to find circles of radius 30 units c) result of using circular Hough transform to find circles of radius 10 units

3.2 Methodology

3.2.1 Edge Detection

Some specific properties of the infant's fundus images are that they are low contrast and very noisy. However, only the edge of the OD's circular shape is needed to calculate the Hough Transform. In order to get rid of noisy and unwanted information, Canny Edge operator was experimentally chosen and applied to the image as the first step in this process. This technique removes most of the noise due to the fine texture leaving only the required edges of the OD. Experimentally, we found that the Canny Operator with the following parameters gives the best result: $\sigma = 1$ and the window size is 5 x 5.

3.2.2 First approximation of Optic Disk

Normal circular Hough transform requires very high computational power because it is needed to form a 3D histogram. We tried to reduce dimensions of the histogram to two dimensions, based on an approximation of the first known OD radius. From our test set of images, statistically, we found that size of most of the OD radii are between 20 pixels and 25 pixels. This prior information can be used to reduce dimensionality of the Circular Hough histogram from 3D to 2D for better accuracy and faster calculation. During the calculation process, the accumulator parameter array are filled according to each of the above radii, where each array composed of cells for the *(x,y)* coordinates of the center of the potential circle. The edge image is scanned and all the points in this space are mapped to Hough space using an Equation (3.2). A value in particular point in Hough space is accumulated if there is a corresponding point in the image space. The process is repeated until all the points in the image space are processed. The resulting Hough transform image was scaled so all the values lie between 0 and 1. Then it was thresholded to leave only those points with high probability of being the centers. Then the different regions were matched by different circles. The output image is computed by drawing circle with these points and adding this to the input image as shown in Figure 3.4. In order to reduce the chance that there is more than one thresholded points staying closed together. The resulting 2D histogram will be sent to dilation and erosion functions, so these points will be combined as one final point.

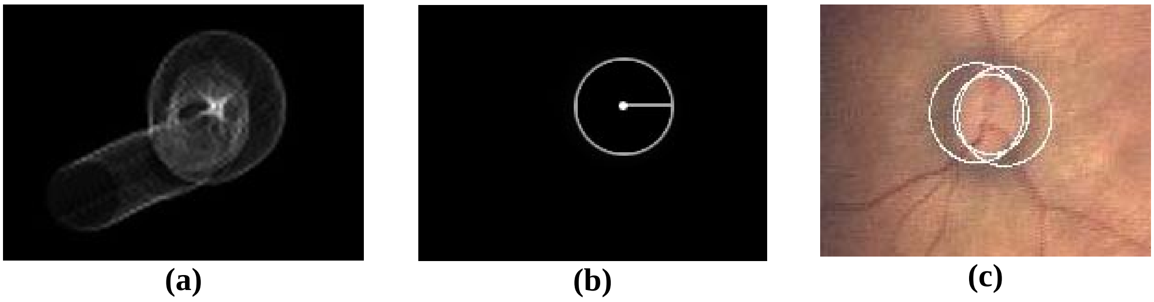
(a) (b) (c)

Figure 3.4 (a) A part of an resulting image after applying 2D circular Hough transform (b) Result of matching the circle to the high probability point with 20-pixel radius (c) First few approximation of circle

3.2.3 Finding Best Circle

A set of approximated circles from the previous step will be compared in this step. The best circles of this set would be the circle that fits most of the OD edges. In this step we counted the number of pixel which is in the vicinity of the detected circle's edge. A mask in a shape of a donut is put on the binary edge image on the same location of each of the detected circle. From the statistical experiment, the best width of the donut ring is five pixels. Number of edge pixels under this mask will be counted and compared for all the detected circles.

The pixel counting is normalized by this formula, $X = \textit{detected pixels} / 2\pi r$, a number of detected pixels divided by the total curriculum of an approximated circle as shown in Figure 3.5. The value shows the percentage of edge pixel being detected. The highest percentage means that the circle is best to use to locate the optic disk.

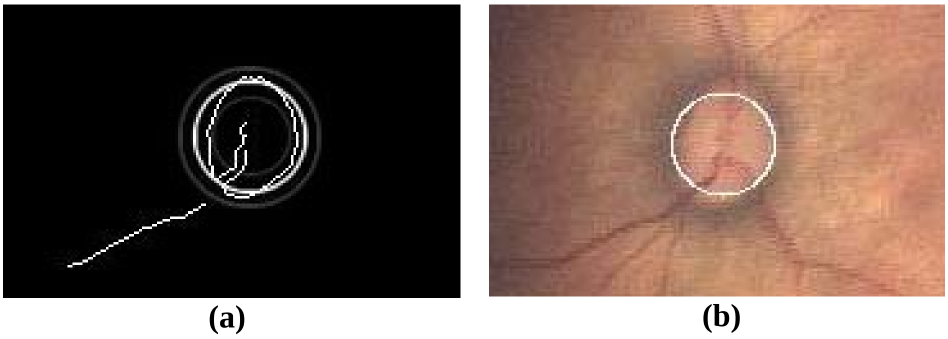
(a) (b)

Figure 3.5 (a) Using a mask shape of donut (b) The best detected circle

3.3 Experimental Verification

The results were clinically validated in this step. All images in our test set are sent to ophthalmologist to identify the OD manually. All the OD's which are automatically detected by our system are then compared with clinician's hand-drawn ground truth. Figure 3.6 shows an example of both ground truth image and our detection result. The hand-drawn and detected optic disk images are represented in white. Number of pixels of the detected image that intersected with pixels of the hand-drawn image will be summed and compared with the number of pixels on the hand-drawn ground truth as demonstrated in Table 3.1.

Table 3.1 The examples of comparison result of intersected pixels on selected images.

Image ID	Image Name	Detected pixels	Ground truth pixels	Accuracy (%)
1	A1	1152	1175	98.5
2	A2	1215	1332	95.1
3	A11	1236	1312	94.2
4	A12	1295	1401	92.4
5	A13	1261	1416	89.1
6	A14	1125	1470	76.5
7	A15	1257	1510	83.2
8	A16	1205	1549	77.8
9	A17	1243	1567	79.3
10	A19	1363	1661	82.1
11	A20	1315	1809	72.7
12	A3	1047	1177	89.0
13	A5	1325	1530	86.6
14	A7	1291	1470	87.8
15	A8	1248	1538	81.1
16	B2	1301	2015	64.6
17	B3	1109	1281	86.6
18	B5	1227	1517	80.9
19	B7	1259	1542	81.6
20	B8	1240	1497	82.8
21	B9	1267	1663	76.5
22	B10	1315	1531	85.9
23	B11	1224	1558	78.6
24	C2	1404	1565	89.7
25	C5	1362	1374	99.6
26	C7	1286	1582	81.3
27	D14	1262	2107	59.9
28	E1	1291	1914	67.5
29	E3	1184	1836	64.7
30	D6	1129	1644	68.7
31	C8	1273	1598	79.7
32	C10	1207	1536	78.9
33	C11	1124	1319	85.2
34	C12	1150	1331	86.4
35	C13	1199	1380	86.9
36	C14	980	1137	86.2
37	C20	1634	2094	78.0
38	D2	1143	1360	84.0
39	D4	1188	1495	79.5
40	D7	1158	1370	85.0
41	D8	1225	1531	80.0
42	D10	1545	1792	86.6
43	D12	2610	3410	76.5
44	D13	2521	2530	99.6
45	E7	1158	1354	85.5
46	G1	1276	1712	74.5
47	G2	1305	1954	66.8
48	G3	1235	1532	80.6
49	E13	1363	1669	82.0
50	G4	1253	1791	70.0
Overall				**81.7**

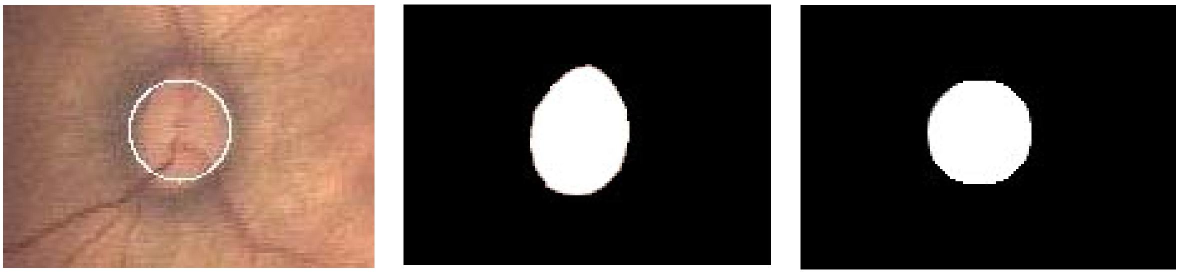

(a) (b) (c)

Figure 3.6 (a) OD automatically detected by our system (b) Clinician's hand-drawn ground truth (c) Detected pixels

All of the processes are concluded with a flow chart in a Figure 3.7.

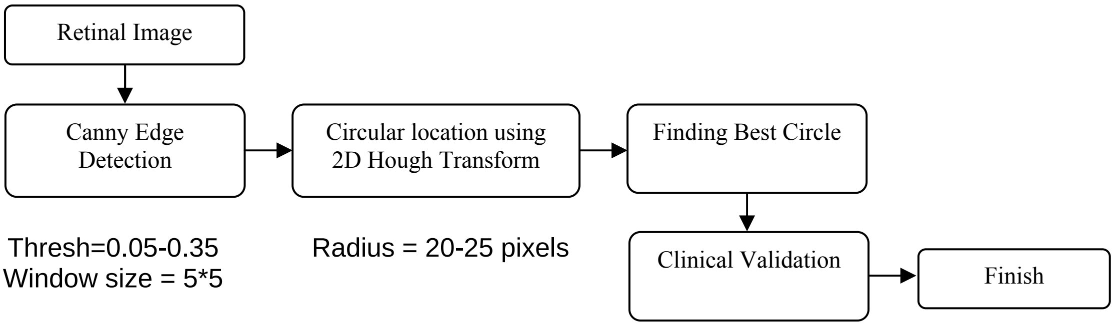

Figure 3.7 Showing a flowchart of 2D Circular Hough Transform process

3.4 Experimental Results

The method is tested using a randomly selected set of fifty images. The accuracy result is demonstrated by a graph in Figure 3.8. The chart represents the OD performance evaluation for each image. We found that the average of the accuracy by this method is 81.7 % and the total processing time is 12 seconds for each image with 3 GHz Pentium 4 machine.

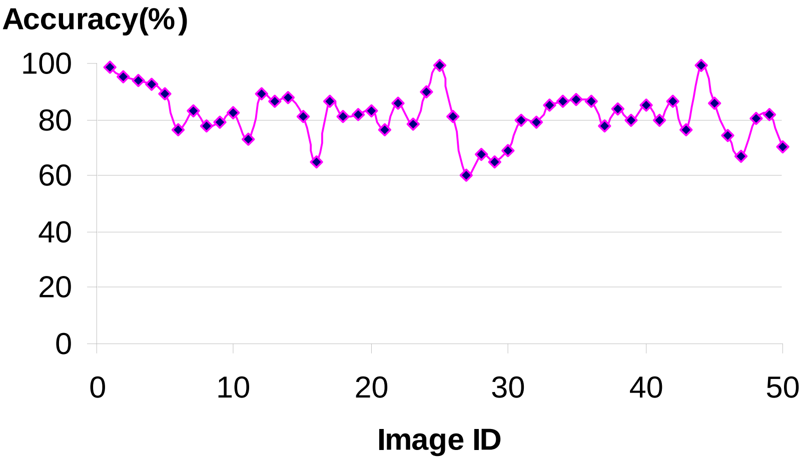

Figure 3.8. Showing the accuracy result of 2D Circular Hough Transform technique

3.5 Conclusion and Discussion

This method is based on canny edge detection and circular Hough transform technique. A prototype has been implemented in MATLAB 7.0.4(R14) on a 3GHz PC under Windows XP. It was tested using a data set of fifty infant's fundus images. From this experiment, the rate of optic disk detection for each image is 12 seconds. The OD position was considered correctly detected if the pixels in the detected image present in the clinician's hand-drawn ground truth. This method was able to locate the position of OD with a high 81.7% accuracy. This technique works pretty well even though the input image is in a low-contrast condition.

Chapter 4

Automatic Optic Disk Detection from Low Contrast Retinal Images of ROP Infant Using GVF Snake

This chapter presents an algorithm for segmentation of optic disk boundary in low-contrast images. The optic disk localization is achieved using segmentation by an active contour model (or Snake) with gradient vector flow (GVF) as an external force. The first snake is place at a location very close to the center of the optic disk approximated by PCA based model. The algorithm is evaluated using fifty retinal images from infants with retinopathy of prematurity(ROP) condition. The results from GVF method were compared with conventional optic disk detection using 2D Circular Hough Transform and later verified with hand-drawn ground truth. The overview of Principal Component Analysis(PCA) and active contours, materials and method, experimental verification, experimental results, conclusion and discussion are included in the this chapter.

4.1 Overview of Principal Component Analysis (PCA)

Karhaunen-Loeve Transform or Principal Component Analysis (PCA) has been a popular technique for many image processing and pattern recognition applications. This transform which is also known as Hotelling Transform is based on the concepts of statistical properties of image pixels or pattern feature. Principal component analysis (PCA) forms the basis of the Karhunen-Loeve(KL) transform for compact representation of data. The KL transform and the theory behind the principal component analysis are the fundamental importance in signal and image processing. The principal has also found its place in data mining for reduction of large dimensional datasets. It has been successfully applied to text analysis and face recognition as well. One of the major problems in pattern recognition and image processing is the dimensionality reduction. In practical pattern recognition problems, quite often the features that we choose are correlated with each other and a number of them are useless so far as their discriminability is concerned. If we can reduce the number of features, i.e., reduce the dimensionality of the feature space, then we will achieve better accuracy with lesser storage and computational complexities (Acharya and Ray, 2005).

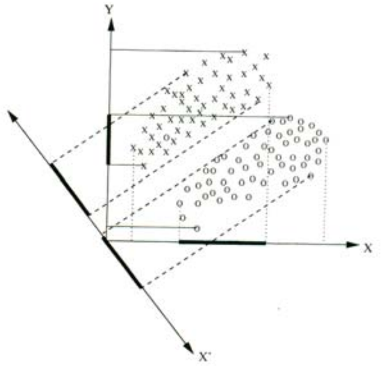

Figure 4.1 Dimensionality Reduction

Figure 4.1 shows a number of two-dimensional pattern points, belonging to two different pattern classes (shown by X and O symbols), where each pattern is described by only two features X and Y. It may be observed that the projection of the pattern points both on X and Y axes are overlapping. As a result, the two features X and Y do not exhibit good discriminability. It is possible to find a reduced set of features that may result in better discrimination between the two classes. This is shown by the non-overlapping projections of the patterns belonging to two classes on the new feature axis(X') as shown in Figure 4.1 PCA is one such tool which yields an extremely powerful technique for dimensionality reduction and many image processing applications such as compression, classification, feature selection, etc. Before describing the PCA, we would briefly present the concepts the covariance matrix.

4.1.1 Covariance Matrix

In practical pattern recognition problems there are usually more than one feature. During the process of statistical analysis of these data, we have to find out whether these features are independent of one another. Otherwise there exists a relationship between each pair of features. For example, while extracting the features of human face, one may choose two feature such as (1) X to denote the distance between the centers of the two irises, and (2) Y to denote the distance between the centers of the left and right eyebrows. From a large set of human faces, we can determine the mean and the standard deviation of the above two features. The standard deviation for each of the above two dimensions of the face data set may be computed independently of each other. To understand whether there exists any relationship between these two features, we have to compute how much the mean of the second feature Y. This measure, which is computed similar to variance, is always measured between two features. The covariance is computed as follows:

$$Cov(X,Y) = \sum_{i=1}^{n} (X_i - \bar{X})(Y_i - \bar{Y}), \qquad (4.1)$$

where n is the number of facial patterns, and $\bar{X}$ and $\bar{Y}$ are the mean of feature X and Y respectively.

If the covariance value is positive, it implies that when one feature (X) increase, the other feature(Y) also increases. If the value of Cov(X,Y) is negative, then as one feature increases, the other one decreases. In case where there is no correlation between the two features are independent of each other. In the problem of face feature selection then one may find that the features have position covariance, meaning that if X increases the other feature Y also increases. In case of a multi-dimensional feature vector, the covariance is measured between each pair of features. In practical pattern recognition problems, we compute a covariance matrix, where each element of the matrix gives a measure of the covariance between two features (Acharya and Ray, 2005).

4.1.2 Eigenvectors and Eigenvalues

In principal component analysis, the concept of eigenvectors and eigenvalues has to be explained. Let us assume that we have a square matrix A of dimension n x n, which when multiplied by a vector X of dimension n x 1 yields another vector Y of dimension n x 1, which is essentially the same as the original vector X that was chosen initially. Such a vector X is called an eigenvector which transforms a square matrix A into a vector, which is either the same vector X or a multiple of X (i.e., a scaled version of the vector X). The matrix A is called a transformation matrix, while the vector X is called an eigenvector. As is well known, any integer multiplication of the vector results in the same vector pointing to the same direction, with only its magnitude being scaled up (i.e., the vector is only elongated).

It is interesting to note here that eigenvectors can be determined only from the square matrices, while every square matrix does not necessarily yield an eigenvector. Also an n x n square transformation matrix may have only n number of eigenvectors. All these eigenvectors are perpendicular or orthogonal to each other. Every eigenvector is associated with a corresponding eigenvalue. The concept of an eigenvalue is that of a scale which when multiplied by the eigenvector yields the same vector in the same direction (Acharya and Ray, 2005).

4.2 Overview of Active Contours(or Snakes)

Active contour, known as Snake, is the segmentation technique to detect the boundary of interest in an image. Snakes are widely used in detection object boundary shape as well as for tracking a moving object in an image sequence. It is an elastic contour which is fitted to features detected in an image. The nature of its elastic energy draws it more of less strongly to certain preferred configurations, representing prior information about shape which is to be balanced with evidence from an image. Thus Snake is an energy-minimizing spline guided by external constraint forces and influenced by image forces that pull it towards features such as lines and edges. Snakes lock onto nearby edges, localizing them accurately (Kass *et al*, 1987; William and Shah, 1992).

Snakes have been used for edge and curve detection, segmentation, shape modeling and visual tracking. It is parametric curve and its properties are specified through a function called energy functional. A partial differential equation controlling the snake causes it to evolve so as to reduce its energy. The motion of the snake is caused by simulated forces acting upon it. The snake is a curve defined by $v(s,t)=[x(s,t),y(s,t)]$ in the x-y image plane, where s is a parameter corresponding on the curve, $s\in[0,1]$, and t as time.

In order to find the position of snake, the energy functional E_{snake} is represented as a sum of internal energy and external energy

$$E_{snake}=\int_0^1[E_{\text{int}}(v(s,t))+E_{ext}(v(s,t))]ds \qquad (4.2)$$

where $E_{\text{int}}(v)$ represents the internal energy of the contour, and $E_{ext}(v)$ represents the external energy.

Gradient vector flow or GVF forces were then chosen because they derived from a diffusion operation and they tend to extend very far away from the object (Xu and Prince, 1998). The gradient vector flow (GVF) snake begins with the calculation of a field of forces, called the GVF forces, over the image domain. The GVF forces are calculated by applying generalized diffusion equations to both components of the gradient of an image edge map. The distance potential force is based on the principle that the model point should be attracted to the nearest edge points. This principle, however, can cause difficulties when deforming a contour or surface in to boundary concavities. Xu and

Prince(1998) employed a vector diffusion equation that diffuses the gradient of an edge map in regions distant form the boundary, yielding a different force field called gradient vector flow (GVF) field. The amount of diffusion adapts according to the strength of edges to avoid distorting object boundaries.
The gradient vector flow (GVF) field $F_{ext}^{GVF} = h(x,y)$ is defined as

$$F_{ext}^{GVF} = h(x,y) = \begin{pmatrix} p(x,y) \\ q(x,y) \end{pmatrix} \qquad (4.3)$$

The GVF field $h(x,y)$ is defined to minimize the following energy functional:

$$E_{GVF} = \int_x \int_y \left[\lambda \left(\left|\frac{\partial p}{\partial x}\right|^2 + \left|\frac{\partial p}{\partial y}\right|^2 + \left|\frac{\partial q}{\partial x}\right|^2 + \left|\frac{\partial q}{\partial y}\right|^2 \right) + |\nabla g|^2 |h - \nabla g|^2 \right] dxdy \qquad (4.4)$$

where g is an edge map of the image and λ is the parameter governing the tradeoff between the first and second terms in integrand. Based on experiment result, λ is 0.5 for our case. Conversely, near edges, where $|\nabla g|$ is large, the second term is dominant and can be regulated by setting $h \approx \nabla g$ so that the local accuracy is preserved.

GVF is computed as a diffusion of the gradient vectors of a grey-level or binary edge map derived from the image. The resultant field has a large capture range, which means that the active contour can be initialized far away from the desired boundary. The GVF field also tends to force active contours into boundary concavities, where traditional Snakes have poor convergence.

4.3 Materials and Methods

4.3.1 Locating a first Snake with Optic Disk Location Approximation by Principal Component Analysis(PCA)

In order to place the first Snake on an image, the approximate location needs to be found. A Principal Component Analysis (PCA)-based model was chosen to serve this purpose because it is very powerful in the detection of a similar shape to the trained shapes. The PCA-based model has been widely investigated in the application of face recognition (Gong *et al.*, 2000). The problem of optic disk location is similar to face detection in certain respects. The approach includes calculating the eigenvectors from the training images, projecting the new retinal image to the space specified by the eigenvectors and calculating the distance between the retinal image and its projection.

The first step of the PCA-based model is a training procedure to obtain ‘disk space’. Fifty optic disk images are carefully selected as the training set. A square sub-image around the optic disk is manually cropped from each fundus image as training data. The sub-images are resized to L x L pixels and their intensities are normalized to the same range to form a training set. Each training image can be viewed as a vector of L^2. L is the set to 90 in our application because most of the optic disk diameters from our test set are able to fit well into this square. The technique of PCA is applied to the training set to get the modes of variation around the average image. The subspace defined by eigenvectors is termed as disk space. The model obtained by PCA statistical analysis is put to use in the localization of the optic disk in fundus images and explained in full detail as follows:

Step 1: Acquisition of Training Data Set

1.1) Optic disks were manually cropped, scaled to L x L, and normalized. They were converted into a vector Γ_i of length L x L. Fifty images were then transformed to a training set of $\{\Gamma_1, \Gamma_2, \Gamma_3, ..., \Gamma_M\}$ where Γ_i is the vector of L^2 and M is fifty for our case (Figure 4.2).

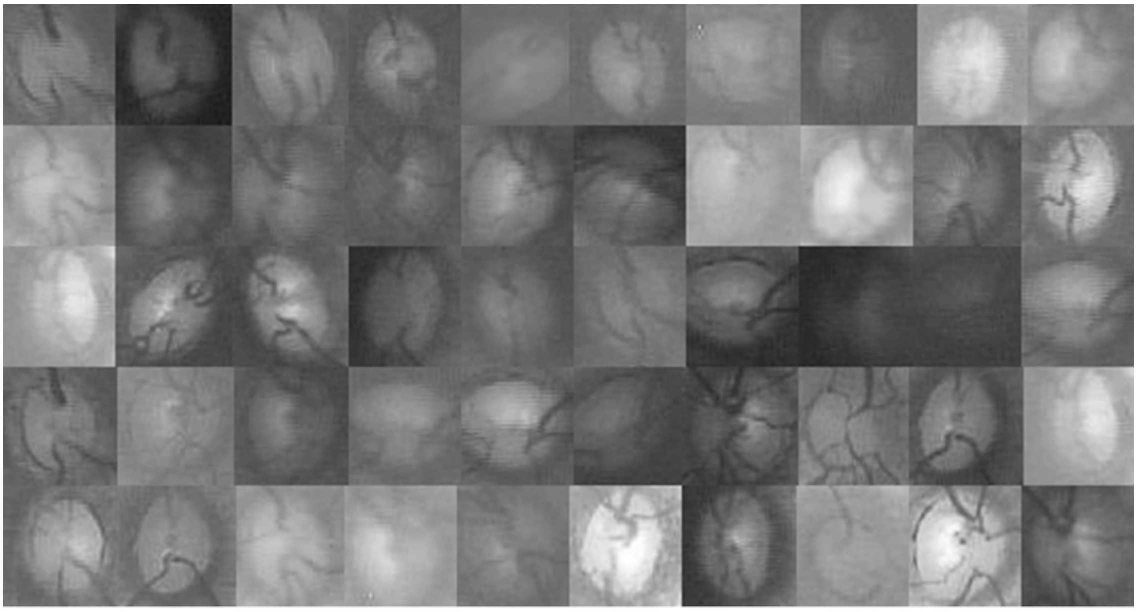

Figure 4.2 The training images of optic disk

Step 2: Definition of Disk Space

2.1) The average vector Ψ was computed using Equation (4.5), as demonstrated in Figure 4.3, and the set of deviation from the average vector $\Phi = [\Phi_1, \Phi_2, ..., \Phi_M]$ is also defined with Equation (4.6)

$$\Psi = \frac{1}{M}\sum_{i=1}^{M}\Gamma_i \tag{4.5}$$

$$\Phi_i = \Gamma_i - \Psi \tag{4.6}$$

where Ψ is the average vector of the training set
Φ is the difference between each training vector and the average vector

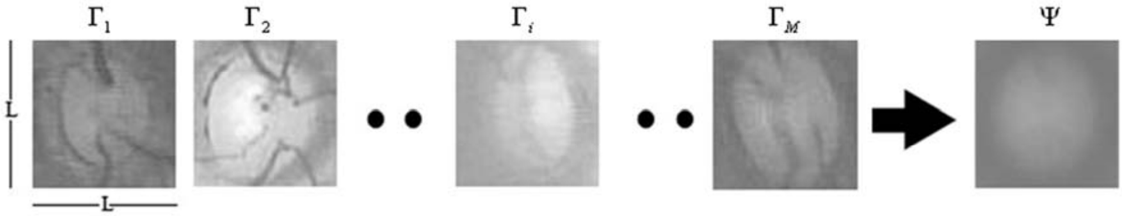

Figure 4.3 The training set of OD image and their average vector

2.2) A covariance matrix C which is defined in Equation (4.7) was computed in this step

$$C = \frac{1}{M}\sum_{i=1}^{M}\Phi_i\Phi_i^T \qquad (4.7)$$

2.3) In this step, the vector u_k, as shown in Figure 4.4, is an eigenvectors (eigen disk) corresponding eigen value λ_k was calculated using Equation (4.8),

$$Cu_k = \lambda_k u_k \qquad (4.8)$$

where u is the eigen vector (eigen disk) of covariance matrix C
λ is The eigen value

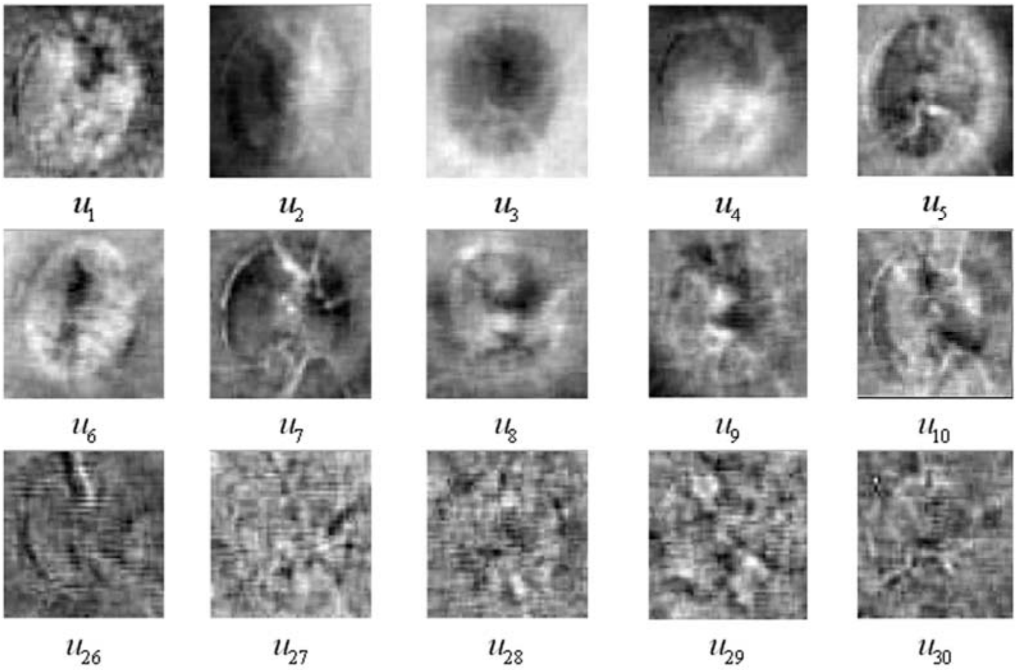

Figure 4.4 The examples of eigen disk

2.4) A test image of original size of 640 x 480 pixels was raster scanned with a united block of L x L to form a Γ_{new}. It is later transformed into the disk space ω_k for k = 1,…,n by the Equation. (4.10). The disk space ω_k forms a vector $\Omega = [\omega_1, \omega_2, ..., \omega_n]$ that describes the contribution of each eigen disk for OD image. Therefore, the simplest method for determining which OD images are identified with new OD image is to find the minimum Euclidian distance by $\varepsilon_i = \|\Omega - \Omega_i\|^2$ and Ω_i is a disk space of i-th OD image of a dataset :

$$\Phi_{new} = \Gamma_{new} - \Psi \qquad (4.9)$$

$$\omega_k = u_k^T \Phi_{new} \qquad (4.10)$$

where $\omega_1, \omega_2 \ldots, \omega_n$ are *n* new disk spaces (Figure 4.5) and *n* is a number of selected dominant eigenvectors.

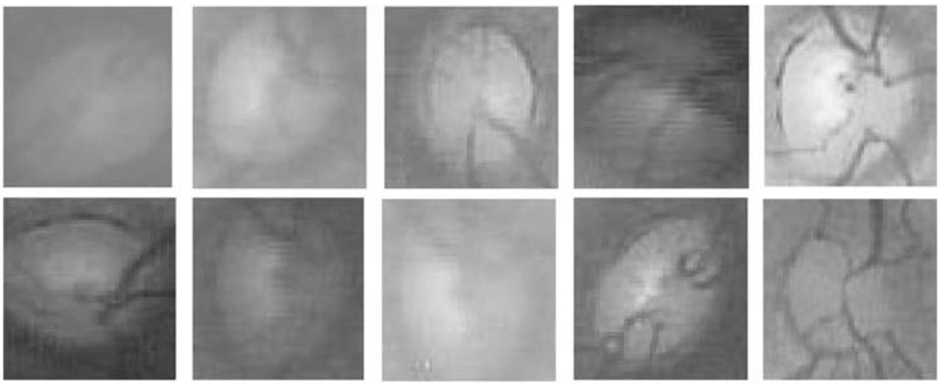

Figure 4.5 Examples of image reconstruction using eigen disk

Step 3: Locating the Optic Disk

3.1) A pre-processed image Φ is reconstructed by using its disk spaces and the eigen disks of the training set as shown in Equation. (4.11)

$$\Phi_r = \sum_{k=1}^{n} \omega_k u_k \qquad (4.11)$$

where Φ_r is a reconstructed image and *n* is the number of dominant eigen disk used in the previous step.

3.2) The sub-image will be classified as OD if the Euclidean distance between Φ_r and Φ_{new}, as expressed in Equation. 4.12, is below a threshold value. The threshold value is derived from $\|\Phi_{new} - \Psi\|^2$. Some example results of optic disk detection are shown in Figure 4.6.

$$\varepsilon_{new} = \|\Phi_{new} - \Phi_r\| \qquad (4.12)$$

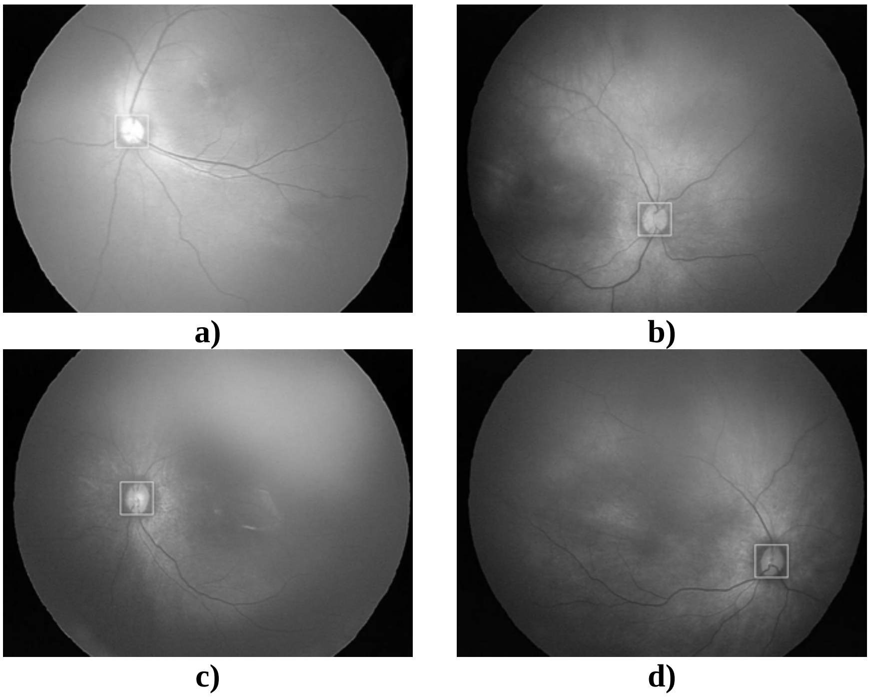

a) b)

c) d)

Figure 4.6 The detection results of four example OD images

A library set of 50 patterns of OD is used in the training process. Fifty retinal images are used for classification. To compute, the average vector in Equation. (4.5), each segmented OD is registered to same orientation. All the processes in this step are summarized by a flowchart in Figure 4.7. The result from this step is quite successful; the algorithm can locate the OD with 80% accuracy compared with manual OD location from a test set of fifty images. The fail outcomes resulted from poor image quality or very blurred and unclassifiable OD.

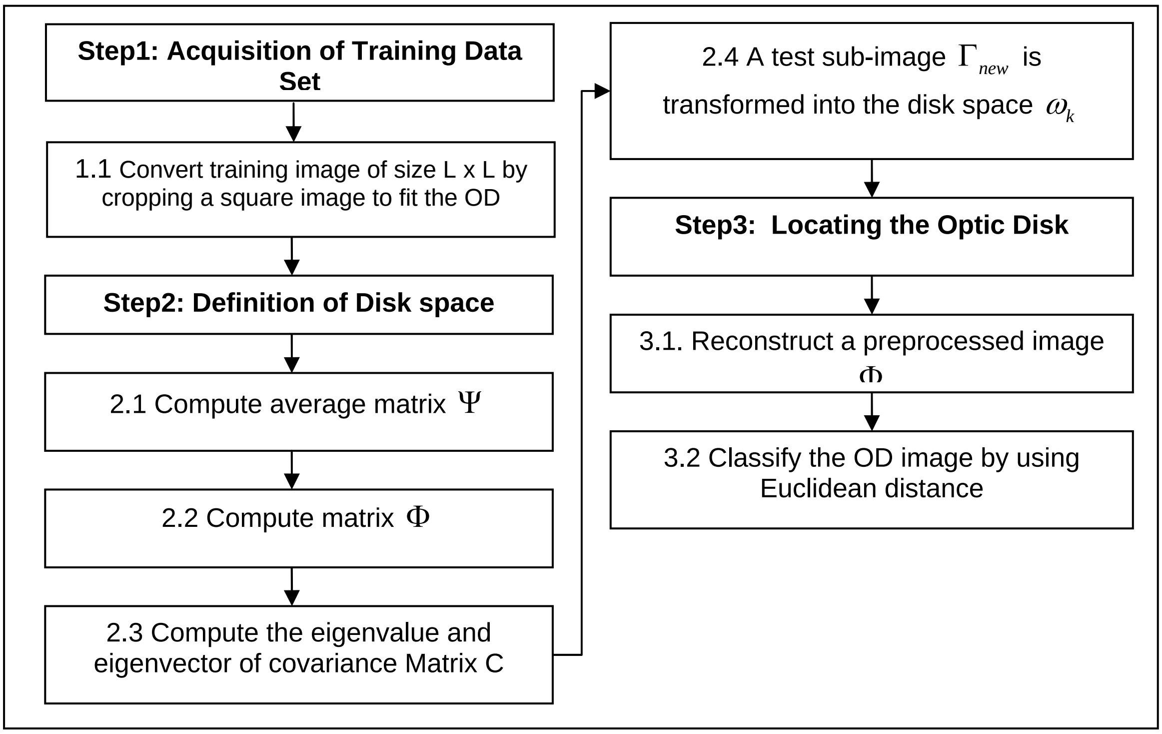

Figure 4.7 Showing a flowchart of PCA

4.3.2 Get actual shape of OD by GVF Snakes

The implementation steps of using a GVF Snake to detect the OD boundary is as follows.

Step 1: The first Snake is placed near the image contour of interest as a result from the previous step. Figure 4.8(a) demonstrated the result.

Step 2: Find the Gradient Image. A simple Gaussian filter was applied on the image in order to get rid of the unwanted noise. This technique removes most of the noise and leaves the edge of OD boundary. Sigma of 2.5 was experimentally chosen. The result from this step is displayed in Figure 4.8(b).

Step 3: Generate GVF Force Field. The edge map was transformed into a gradient vector force field in this step. An external force field or gradient vector flow (GVF) field dense vector field derived from a gradient image by minimizing energy functional in a variation framework (Xu and Prince, 1998). The result from this step is shown in Figure 4.8(c).

Step 4: Snake Deformation. The shape of the Snake begins to deform in every iteration driving by forces applied on them. The iteration is repeated until the Snake is stable, the difference between two consecutive Snakes is lower than a threshold. An example of three steps is shown in Figure 4.8(d,e,f).

Step 5: Map the Resulting Snake to the Original Image. The boundary contour of the detected OD was mapped to the original image, as shown in Figure 4.8(g,h). This will facilitate the clinician’s decision.

The whole process is summarized in Figure 4.9 and six more successful results are shown in Figure 4.10.

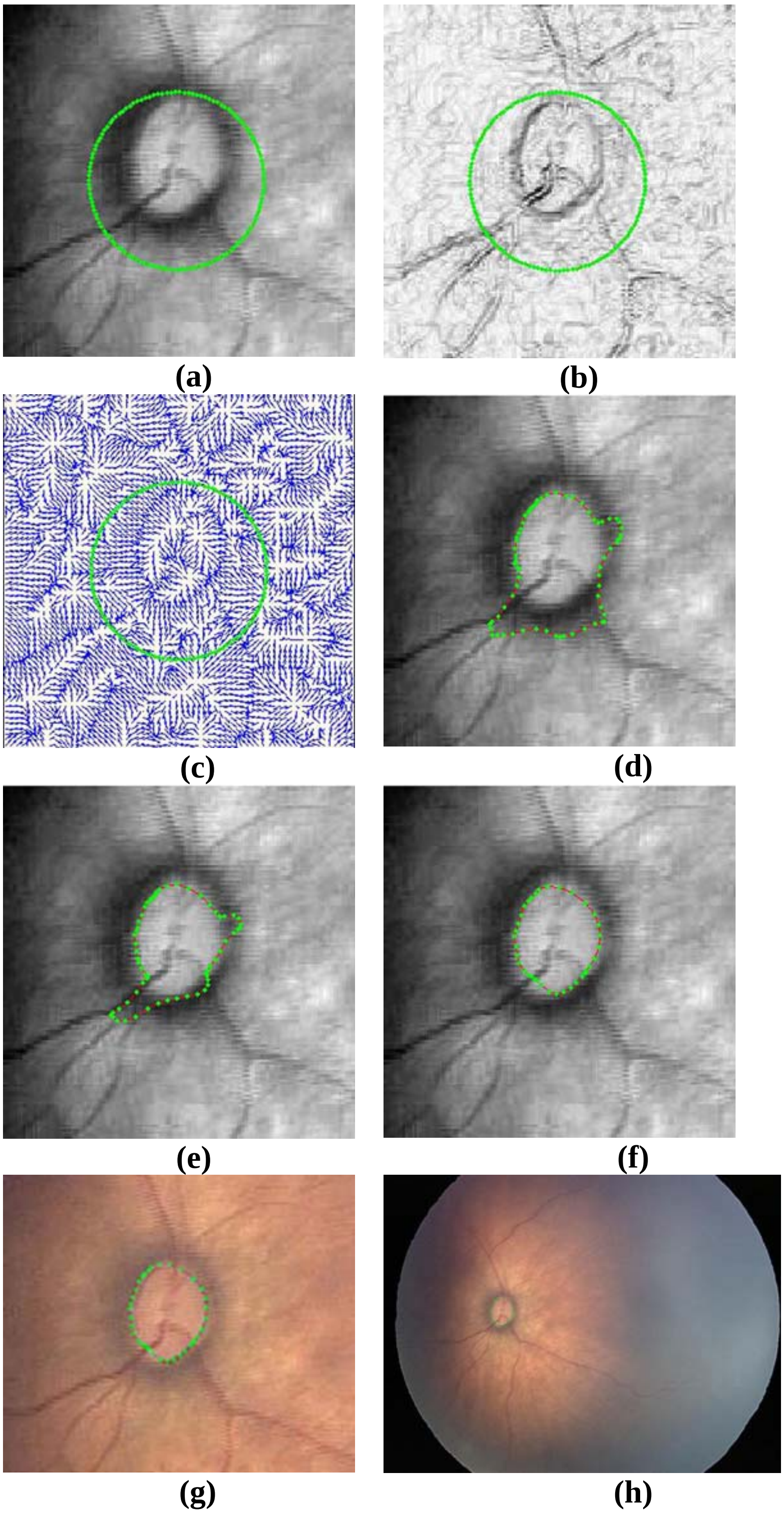

Figure 4.8 (a) The first Snake is placed near OD (b) The edge map $|G(x,y)*I(x,y)|^2$ with sigma = 2.5 (c) GVF field image (d), (e), (f) An example of GVF Snake in action where (d) Initial position of Snake and location of the model after 40 (e) 80 and (f) 200 iterations (g), (h) Detected OD is mapped to the original fundus image

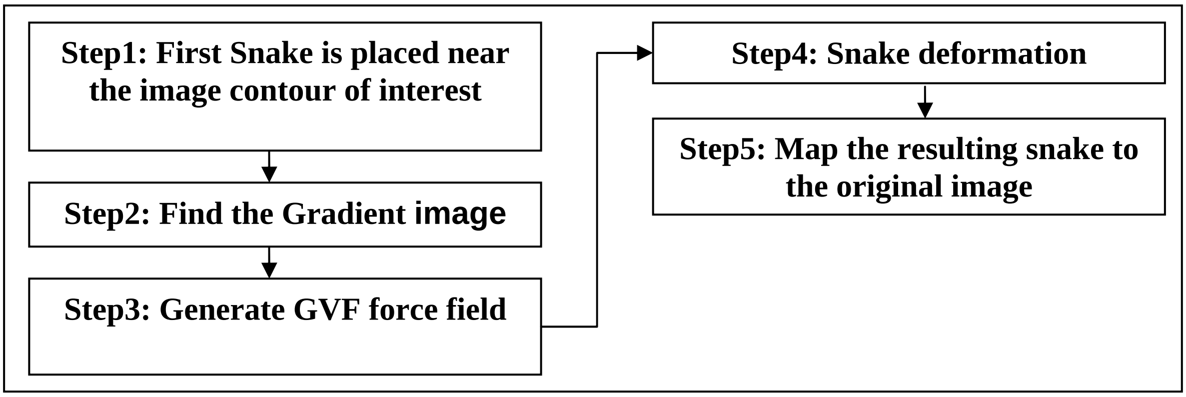

Figure 4.9 Showing a flowchart of GVF Snake

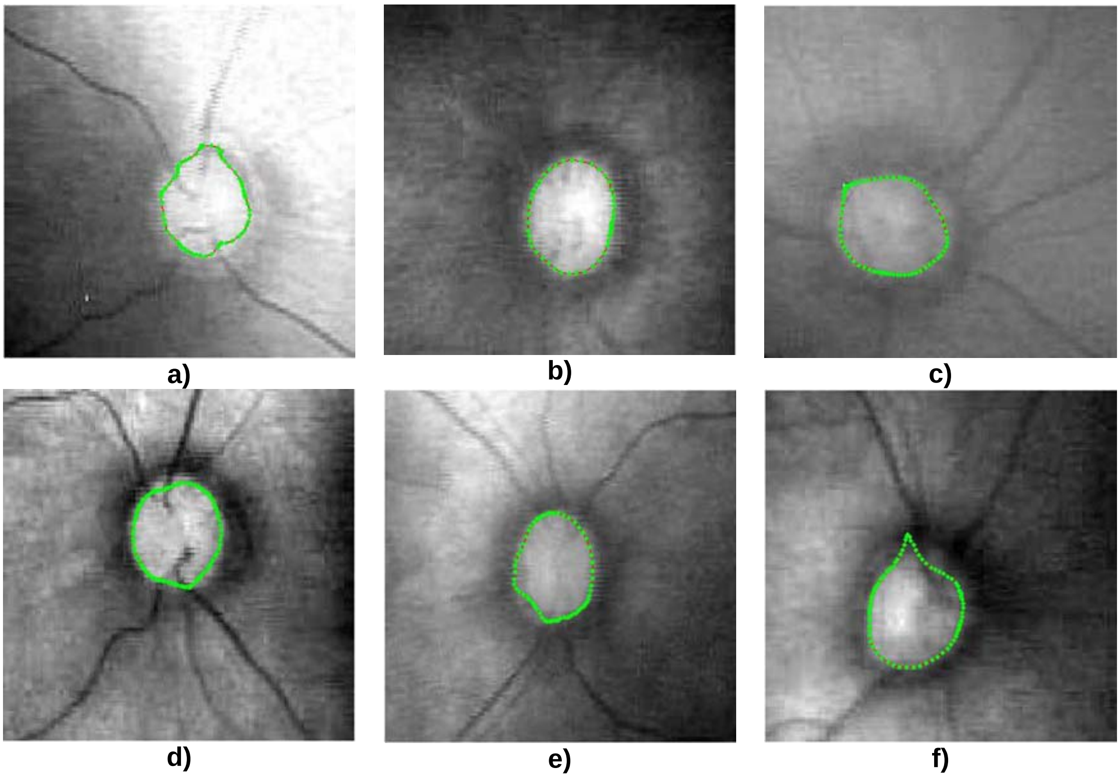

Figure 4.10 Examples of successful results

4.4 Experimental Verification

The results were clinically validated in this step. All images in our test set were sent to an ophthalmologist to identify the OD manually. The expert ophthalmologist hand-labeled the optic disk on the screen. All optic disk pixels were set to white, and all non-optic disk pixels were set to black. The new image was saved as a ground truth which will be used for comparison. All the OD's which are automatically detected by our system are then compared with the clinician's hand-drawn ground truth. Figure 4.11 shows an example of both the ground truth image and our detection result. The hand-drawn and detected optic disk images are represented in white. The number of detected pixels that intersect with pixels of the hand-drawn ground truth will be summed and calculated as a percentage of pixels on the hand-drawn ground truth, as demonstrated in Table 4.1.

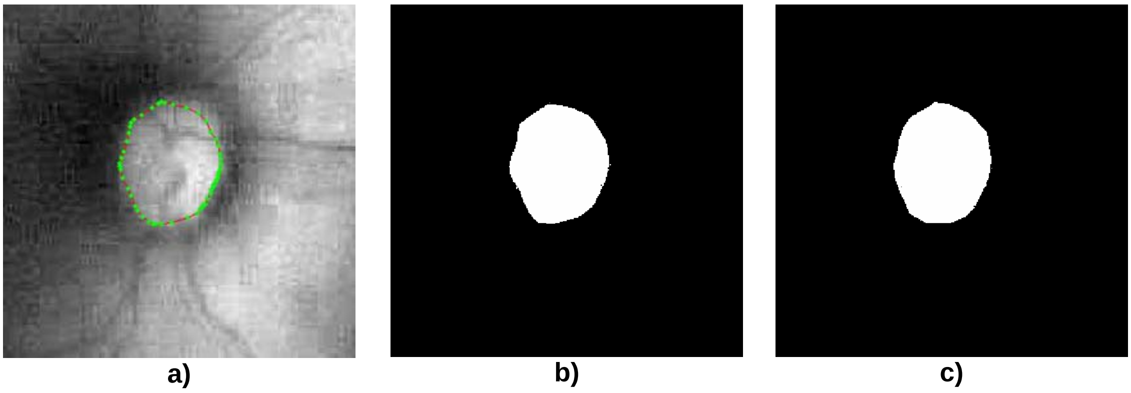

Figure 4.11 (a) OD automatically detected by our system (b) Detected pixels (c) Clinician's hand-drawn ground truth

Accuracy Measurement

To evaluate the performance of the algorithm quantitatively, the measure of accuracy is defined as follow:

$$\text{Accuracy} = \frac{(TP + TN)}{(TP + FN + TN + FP)} \times 100 \qquad (4.13)$$

where TP,TN,FP and FN stand for true positive, true negative, false positive and false negative, respectively (Costaridou, 2005). An example of the comparison is demonstrated in Figure 4.12.

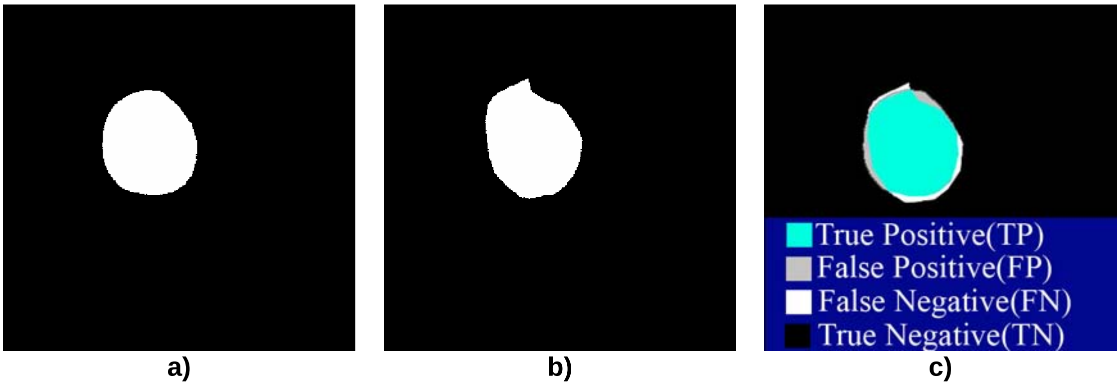

Figure 4.12 (a) ground truth image (b) Detected pixels (c) definition of segmentation evaluation

Table 4.1 The examples of comparison result of intersected pixels on selected images.

Image ID	Image Name	Ground truth pixels	Detected pixels from Snake with GVF	Detected pixels from Hough Transform	Snake Accuracy (%)	2D Circular Hough Transform Accuracy (%)
1	A1	7,891	7,625	7,487	96.6	94.9
2	A2	7,466	6,257	5,896	83.8	79.0
3	A3	6,174	5,474	4,783	88.7	77.5
4	A5	8,628	6,181	0	71.6	0.0
5	A6	7,453	5,890	5,763	79.0	77.3
6	A7	8,658	7,624	7,526	88.1	86.9
7	A9	5,470	5,321	5,240	97.3	95.8
8	B2	14,481	10,670	8,401	73.7	58.0

Image ID	Image Name	Ground truth pixels	Detected pixels from Snake with GVF	Detected pixels from Hough Transform	Snake Accuracy (%)	2D Circular Hough Transform Accuracy (%)
9	B3	12,649	10,943	7,216	86.5	57.1
10	B6	7,099	5,230	0	73.7	0.0
11	B8	9,254	8,728	7,576	94.3	81.9
12	B10	9,203	7,878	0	85.6	0.0
13	C2	8,393	7,373	7,236	87.9	86.2
14	C5	7,776	5,927	7,462	76.2	96.0
15	C6	8,587	7,441	7,135	86.7	83.1
16	C7	8,438	6,278	0	74.4	0.0
17	C8	7,879	6,330	0	80.3	0.0
18	C9	7,520	6,469	0	86.0	0.0
19	C10	7,615	6,842	2,544	89.9	33.4
20	C11	7,551	6,356	0	84.2	0.0
21	C12	7,509	6,228	0	82.9	0.0
22	C13	8,155	6,612	0	81.1	0.0
23	C14	6,494	5,863	0	90.3	0.0
24	D1	7,029	6,010	0	85.5	0.0
25	D3	14,175	11,002	7,291	77.6	51.4
26	D4	8,513	7,113	0	83.6	0.0
27	D11	8,937	7,213	0	80.7	0.0
28	D14	10,644	9,854	0	92.6	0.0
29	E2	7,517	5,270	7,037	70.1	93.6
30	E3	9,581	7,674	7,268	80.1	75.9
31	E6	14,075	9,854	7,356	70.0	52.3
32	E7	8,077	7,298	7,360	90.4	91.1
33	E9	9,935	7,710	7,267	77.6	73.2
34	G1	9,096	8,761	7,268	96.3	79.9
35	G2	9,682	7,747	7,296	80.0	75.4
36	G3	9,611	9,036	7,221	94.0	75.1
37	G4	9,484	8,978	3,703	94.7	39.0
38	G5	8,648	8,497	7,180	98.3	83.0
39	G6	9,768	7,885	7,147	80.7	73.2
40	G8	7,004	5,782	5,521	82.6	78.8
41	G9	7,929	6,864	7,375	86.6	93.0
42	G10	6,670	5,562	5,320	83.4	79.8
43	G11	7,147	5,769	5,478	80.7	76.7
44	G12	7,872	6,704	7,172	85.2	91.1
45	G14	6,220	5,622	5,312	90.4	85.4
46	G15	7,685	7,577	7,303	98.6	95.0
47	G16	7,882	7,108	7,193	90.2	91.3
48	G17	7,435	7,097	7,113	95.5	95.7
49	G18	7,622	7,154	7,558	93.9	99.2
50	G19	8,057	7,182	7,138	89.1	88.6
				Average Percentage	85.3	56.9

4.5 Experimental Results

Fifty images with varying shapes and sizes of optic disk were used in this process. These fifty images represent most of the cases of the ROP symptoms and they were sufficiently used to prove the concept of this algorithm. If the system is to be used in real situation, a bigger number of the images would be required. Apart from segmentation results from the GVF Snake, for comparison purposes, we also processed this set of images using a simpler 2D Circular Hough Transform. (This technique is based on a circular Hough Transform and the dimensions of the normal circular Hough Transform histogram are reduced from 3 to 2 dimensions by assuming that the approximate OD radius is known. Only the first few circles are evaluated by using the maximum point from Hough space). The detail of percentage of accuracy is shown in Figure 4.13.

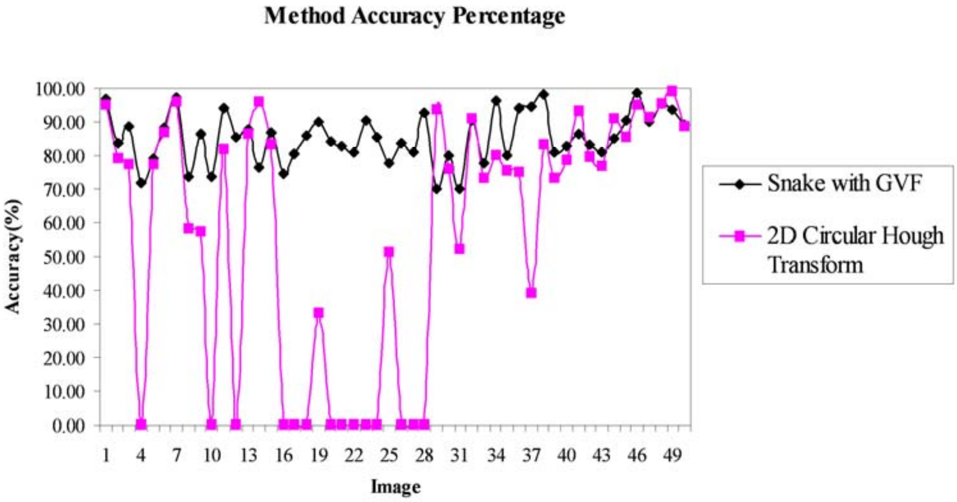

Figure 4.13 The accuracy result for all images

4.6 Conclusion and Discussion

We have presented a method for optic disk detection based on a PCA and GVF Snake. The method was implemented on Pentium 4, 3GHz machine with 1 GB of RAM and the speed of transform is approximately 10 seconds/image. Because the algorithm will stop when there are no changes in the accuracy, i.e. when the result is converged. From our experiment, approximately it will converge after 10 second for each image. The Rate of Convergence for each image is 10 seconds with 3 GHz Pentium 4 machine. The PCA was used to get a rough location of the OD, and the first GVF Snake was placed closely to the center of the optic disk. The GVF Snake then followed the external vector force field until it fitted the boundary of the OD. The results were compared with the result from a 2D Circular Hough Transform and validated against a clinician's hand-drawn ground truth. The accuracy result is quite successful with accuracy of 85.3% compared to the accuracy result of Circular Hough Transform which is 56.9%. One visible advantage of this method is that the ODs are detected even though the boundary of the OD is not continuous or blurred.

Chapter 5

Automatic Optic disk Detection from Low Contrast Retinal Images of ROP Infant Using Mathematical Morphology

In this chapter, we present the algorithm that is effectively detected optic disk from the infant's retinal images. The algorithm is based on mathematical morphology technique to extract the optic disk from the retinal image. In addition, the overview of mathematical morphology, materials and method, result verification, experimental results and conclusion and discussion are included in this chapter.

5.1 Overview of Mathematical Morphology

Mathematical morphology has its origins in set theory and concerns the study of form and structure. Within image analysis it concerns the shape and properties of objects, or regions of an image, and how these may be changed, and useful features extracted.

While the formal mathematics of set theory utilizes concepts of set inclusion, complement, union and intersection, a useful insight into the topic of morphology can be achieved using a more intuitive approach based upon plain English descriptions of operations performed and the logical expressions OR, AND and NOT. In addition the familiar operation of moving a template, or mask, over an image and performing specific template-image comparison at each template position will give similar results to the set theoretical approach (Awcock and Thomas, 1996).

5.1.1 Erosion and Dilation

Two operations which are fundamental to morphological analysis of images are 'erosion' and 'dilation'. Almost all morphological operations can be defined in terms of these two basic operations.

Erosion of set A by structuring element B is denoted $A\Theta B^t$ and is formally defined mathematically as

$$A\Theta B^t = \left\{ p \mid B_p \subset A \right\} \qquad (5.1)$$

where B^t is the transposed form of the structuring element set, and

B_p represents the structuring element centred at poing p

However, since the erosion operation is based on inclusion it is more simply conceived of as the output set obtained where the template is completely contained by the image set. Thus the eroded image of Figure 5.1 is produced by stepping the structuring element, or template, over the input until ALL of the foreground pixels of the template fit over foreground pixels in the underlying image. At each position where this is true a pixel is written to the output array corresponding to the reference pixel position, *p*. This is equivalent to hit-miss transformation of the image with the structuring element, where there are NO background pixels in the latter – i.e. $B_{bgd} = \varnothing$. Notice how erosion enlarges holes in the object, shrinks its boundary, eliminates 'islands' and removes narrow ‘peninsulas’ that might exist on the boundary. Also consider the effect of eroding the object with a 3x3 grid of foreground pixels, F, and then finding the morphological difference between this and the original object. The result is a row of connected single pixels corresponding to the outermost extreme of the object foreground – a perfect boundary, known as the ‘inner’ boundary of the object. For the record this is expressed mathematically as

$$\text{Inner boundary} = A / A\Theta F \qquad (5.2)$$

Dilation is the ‘dual’ of erosion, that is, the dilation of a set A is equivalent of the erosion of the complement set A*. Therefore, dilation, denoted $A \oplus B^t$, may be defined as

$$A \oplus B^t = A^* \Theta B^t \qquad (5.3)$$

This mathematical notion of duality means that dilation can be performed by eroding the complement set by the same structuring element. In practice, this means that a foreground object in a binary image can be dilated by eroding the background with the same structuring element. Alternatively dilation is formally defined mathematically as

$$A \oplus B^t = \left\{ p \mid B_p \cap A \neq \varnothing \right\} \qquad (5.4)$$

This means that an output pixel will be written at all points where the translated structuring element ‘hits’ the image set –i.e. they have a ‘non-empty intersection’.

Stated more intuitively, the mathematical definition of dilation says that a foreground pixel will be written to the output set at all positions of the structuring element reference where ANY foreground pixel in the structuring element overlays a foreground pixel of the image set (i.e. part of an object). The result of this operation is illustrated in Figure 5.1.

Notice how dilation fills in holes in the object and expands its boundaries, filling in any narrow ‘creeks’ that might exist.

In both Figures 5.1(c) and 5.1(d) the shaded regions indicate the change that is produced by the morphological operator. In Figure 5.1(c) the output image is indicated by the solid black area and in Figure 5.1(d) it is indicated by the solid black area PLUS the shaded area. Notice that these operations significantly modify the size of the objects as well as their shape.

5.1.2 Opening and closing

Although dilation and erosion are dual operation it is not possible to reconstruct an image set by application of dilation after previously having eroded the image. The dilation operation will only be able to reconstitute the essential features of the structure of the object as modified by structuring element. However, such a new set can be extremely useful in determining size and shape information. A pair (dual) of sequential operations may thus be formally defined as

‘Opening’, denoted A_B : $\left(A\Theta B^t\right) \oplus B$; i.e. erode then dilate

‘Closing’, denoted A^B : $\left(A \oplus B^t\right)\Theta B$;i.e. dilate then erode

The result of these operations is illustrated in Figure 5.2(b-c). In both cases the original input image is that given above in Figure 5.2(a) and the structuring element is that given in Figure 5.2(b).

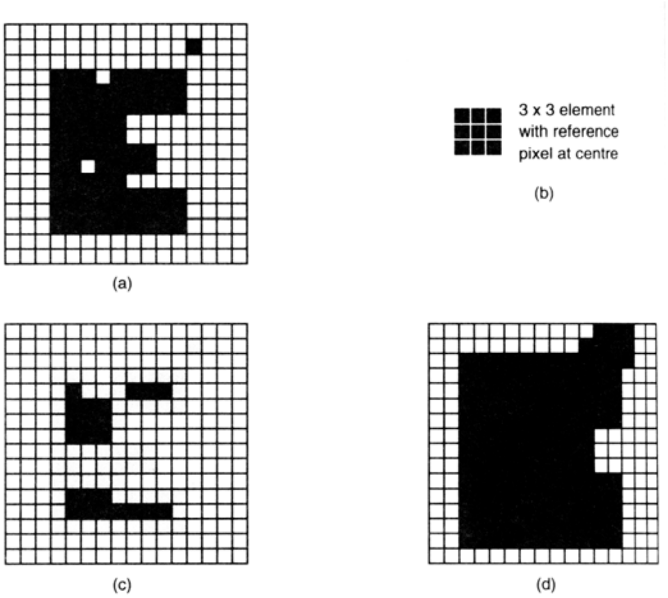

Figure 5.1 Erosion and dilation (a) the original image (black = object) (b) the 3x3 structuring element (c) the erosion of (a) (d) the dilation of (a)

Opening and closing operations form the basis of boundary smoothing and noise elimination process whether the noise is manifest as small holes within the object or as small protrusions external to it. Continuing with the geographical metaphor which seems so appropriate for the effect of morphological operations, opening smoothes object 'coastlines', eliminates small 'islands' and cuts narrow 'isthmuses'. Thus it isolates objects which may be just touching one another, and is therefore a suitable precursor to studies of the distribution of particles sizes –for example, in analysis of wear particles in engine oil, ink particles in recycled paper, or cells in cytology. On the other hand, closing blocks up narrow 'creeks' and small or thin 'lakes' inside the object and links nearby objects. This simplifies the process of assessing the separation of particles.

Note that, while opening or closing significantly modifies the shape of the object, completing these restores the previously eroded or dilated object to their original size.

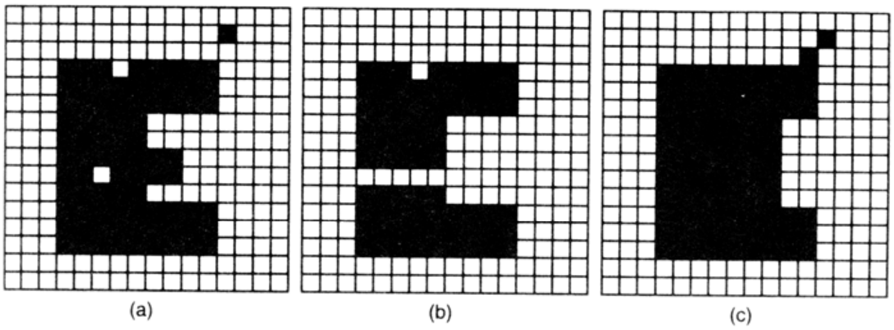

Figure 5.2 Sequential applications of erosion and dilation (a) original image set (b) opened version (c) closed version

5.2 Materials and Methodology

Our approach to detect the optic disk is based on mathematical morphology. The details of all ten steps used in the algorithm are described as follow:

Step 1: Extract Red channel.

The images that we have were taken in low light condition. We found that the strongest color component in these images is the Red component. Furthermore, the color of optic disk always primitive in red channel with round or oval shape in disk. So the red channel was chosen as our input as shown in Figure 5.3(a).

Step 2: Using Histogram Equalization Enhancement

In the infant's retinal image, the image is often blurred. Most of the information is packed in the lower order parts of the image histogram. Improvements in the contrast can make this algorithm more efficient. The image contrast was enhanced by Histogram Equalization to improve the quality of optic disk image.

The transformation is done as a point processing since the enhancement of any pixel is dependent only on red channel at that point. Histogram equalization automatically determines a red channel transformation function that produces an output image with a uniform histogram and improves retinal image contrast as shown in Figure 5.3(b).

Step 3: Average filter

The idea of mean filtering is simply to replace each pixel value in an image with mean value of its neighbors, including itself. This has the effect of eliminating pixel values which are unrepresentative of their surroundings. Average filter is used to remove the unwanted noise in the retinal image as shown in Figure 5.3(c).

Step 4: Morphological Closing

The morphological closing, which is a sliding window operator, was used in this step to remove the dark details from the image, while leaving bright features relatively undisturbed. The effect of the Closing can be applied at this point to remove vessel in the image because the blood vessel will interfere with the result of edge detection in the next step.

Morphological closing is a combination of two fundamental operations, namely dilation and erosion, which is defined by (5.10). Full details of dilation operation and erosion operation are described in step 7 and step 8 respectively.

$$A \bullet B = (A \oplus B) \Theta B \tag{5.10}$$

Result of this step that has smoothes image without blood vessel as shown in Figure 5.3(d).

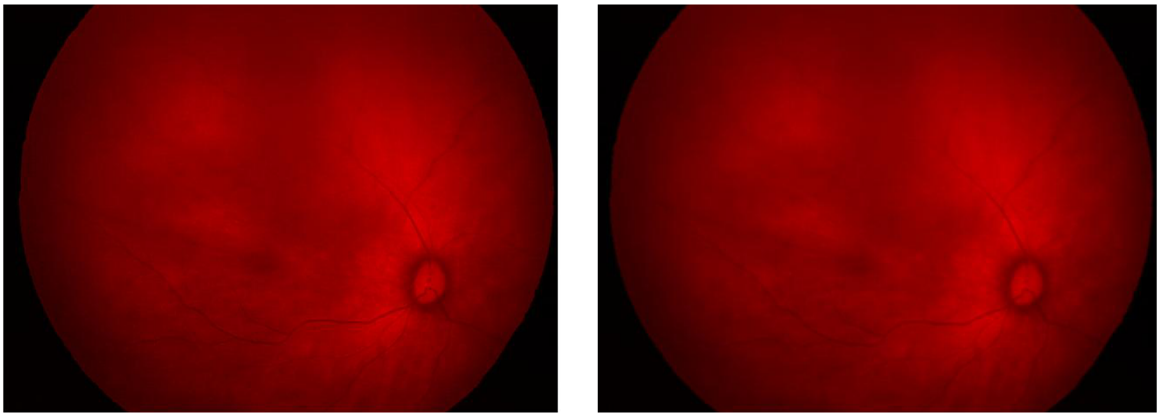

(a) **(b)**

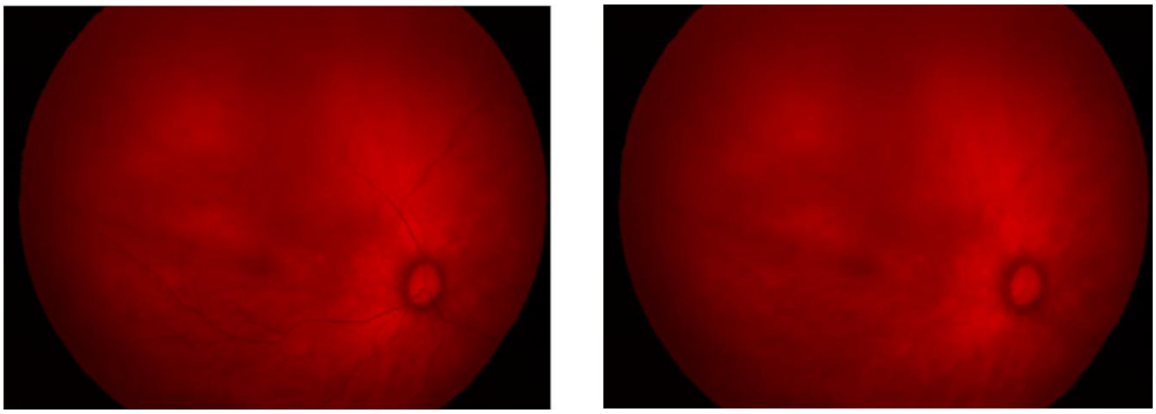

(c) (d)

Figure 5.3 (a) The Optic disk in Red Channel (b) Histogram Enhancement (c) Averaging filter for smoothing the image (d) Closing Image for removing blood vessel

Step 5: Canny edge detection

The Canny edge detection applied to Red channel of RGB to find the edge of the optic disk. The result of this edge detection is a binary image in which the white pixels closely approximate the true edges of the original image as shown in Figure 5.4(a).

Step 6: Thicken the edge

In order to add pixel into the boundary line, convolution mask was applied to give more detail of the edge in optic disk as shown in Figure 5.4(b). The 3 x 3 convolution mask is superimposed upon the input image. The process commenced at the origin and each input pixel is multiplied by the corresponding window value. These nine results are summed and the final value returned to the output image at a position corresponding to the centre element of the window. The window was then moved by one pixel to its next position and the operation was repeated. The filtering operation adds pixels along the edge line in the output image.

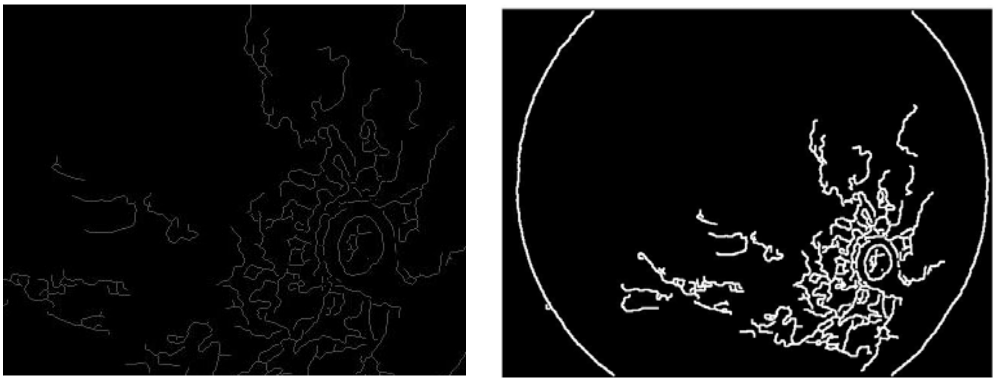

(a) (b)

Figure 5.4 (a) Canny Edge detection (b) Edge thickener result

Step 7: Using Dilation and filling the hole and gap within the image

Two basic morphological operators, namely dilation and erosion, are used in this step. Dilation causes objects to dilate or grow in size by adding pixels to the boundaries of the object in an image, while erosion causes objects to shrink by removing pixels on object boundaries. In our case, we dilated the image using disk-shaped structured element that defines the neighborhood region around its origin with a radius of 5 to connect the region in the image.

The dilation of A by B, denoted by $A \oplus B$, is defined as (5.11)

$$A \oplus B = \{x \mid (\hat{B})_x \cap A \neq \varnothing\} \qquad (5.11)$$

Dilation, which expands the boundary of an object in an image, is achieved by assigning 1 to the origin of the structuring element when it overlaps, even partially, the object. The result of this step in is shown in Figure 5.5(a). Next we developed a simple algorithm for region filling based on set dilations, complementation, and intersections. The objective is to fill the entire optic disk circular region and the other region with 1's in the hole and gap as shown in Figure 5.5(b).

(a) (b) (c)

Figure 5.5 (a) After dilation (b) Fill the hole (c) after image erosion

Step 8: Image Erosion

Erosion contracts the boundary of an object in an image and this effect can be used as one of the steps to separate the optic disk object from other objects. Erosion is achieved by assigning a value one to the origin of the structuring element when it entirely overlaps the object. The result is shown in Figure 5.5(c).

The erosion of A by B, denoted by $A \Theta B$, is defined as(5.12)

$$A \Theta B = \{x \mid (B)_x \subseteq A\} \qquad (5.12)$$

Step 9: Area labeling

In this step we need to separate all the unconnected regions. The areas within the image were separated by labeling using 4-neighborhood connecting. All connected pixels with the same input value are assigned the same identification label. Figure 5.6(a) shows the connected component labeling result.

Step 10: Noise removal

All other comments rather than optic disk are removed in this step. Number of pixels in each individual components in the binary image are counted. From our prior experiment, we manually selected the optic disk from the training set and found that the average number of pixels in the optic disk with the circular shape is in range between 1200 to 1600 pixels. If the number of pixels in a component is not in this range, the components will be removed. The result is as show in Figure 5.6(b). Figure 5.7 presents the example of successful result in the different shape and size of optic disk.

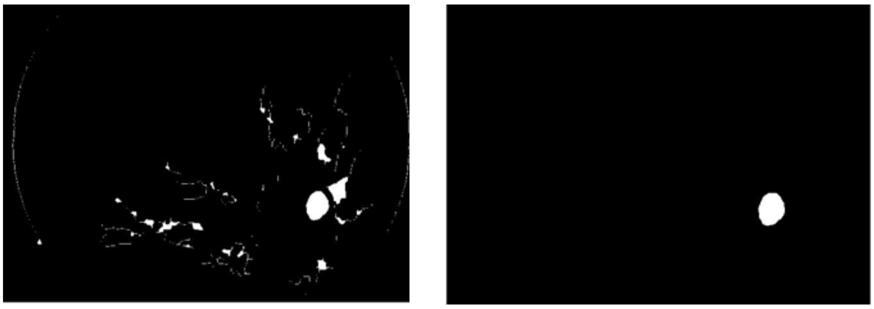

(a) (b)

Figure 5.6 (a) Input image to step 10 (b) After noise removal

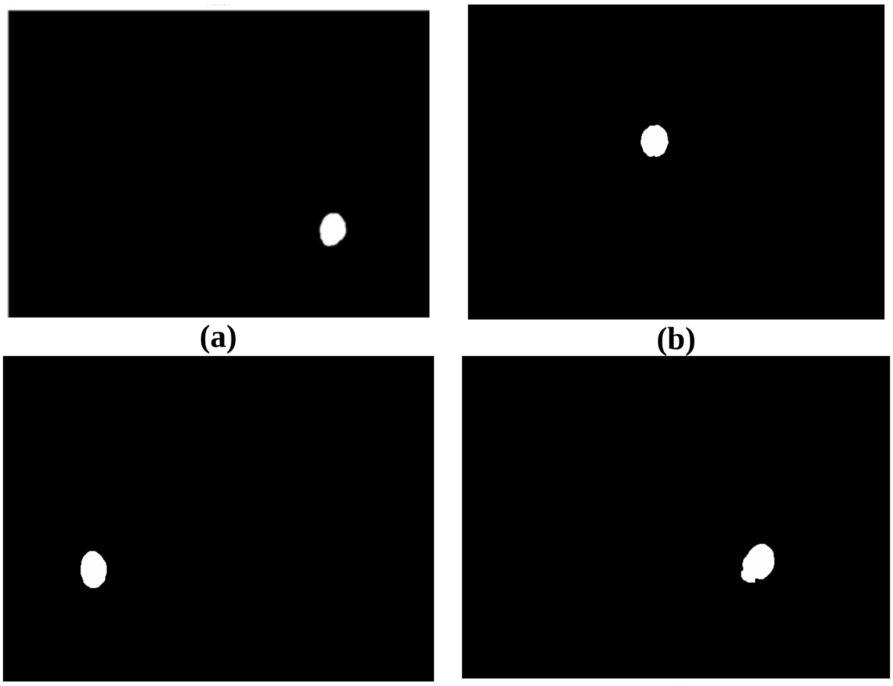

(a) (b)

(c) (d)

Figure 5.7 The examples of successful result

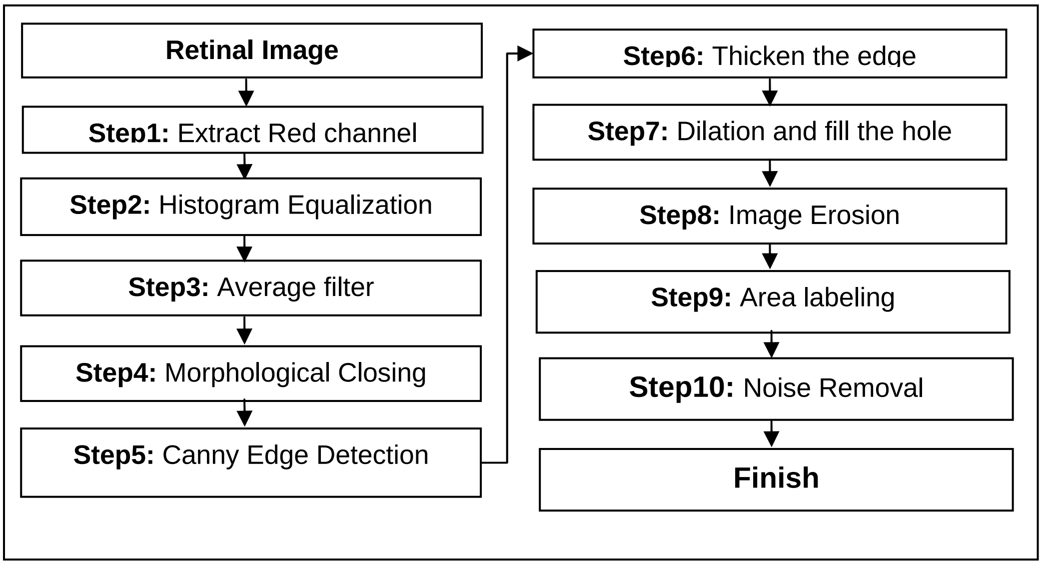

Figure 5.8 Showing the diagram of methodology

5.3 Experimental Verification

The results were clinically validated in this step. All images in our test set were sent to ophthalmologist to identify the OD manually. Expert ophthalmologist hand-labelled the optic disk on the screen. All optic disk pixels were set to white and all non-optic disk pixels set to black. The new image was saved as a ground-truth which will be used for comparison. All the OD's which are automatically detected by our system were then compared with clinician's hand-drawn ground truth. The result is evaluated quantitatively by comparing the resulting detection with ophthalmologists' hand-drawn ground-truth images pixel by pixel. Figure 5.9 shows an example of both ground truth image and our detection result. The hand-drawn and detected optic disk images are represented in white.


(a) **(b)**

Figure 5.9 (a) Clinician's hand-drawn ground truth (b) Detected pixels from mathematical morphology

Four values, namely TP, TN, FP and FN which stand for true positive, true negative, false positive and false negative, respectively (Costaridou, 2005) were used as measurements. True Positive (TP) is a number of optic disk pixels correctly detected, False Positive (FP) is a number of non-optic disk pixels which are detected wrongly as optic disk pixels, False Negative (FN) is a number of optic disk pixels that were not detected and True Negative (TN) is a number of non-optic disk pixels which were correctly identified as non-optic disk pixels as shown in Table 5.1.

Table 5.1 Optic disk verification

	Optic Disk Present	Optic Disk absent
Optic disk detected	True Positive(TP)	False Positive(FP)
Optic disk not detected	False Negative(FN)	True Negative(TN)

In order to evaluate the performance of the algorithm quantitatively, the measure of accuracy, sensitivity, specificity, positive predictive value are also defined (Equation (5.13),(5.14),(5.15) and Equation (5.16)). The accuracy shows the performance of this method, sensitivity shows the proportion of optic disk pixels which positively detected, the specificity shows the proportion of non-optic disk pixels which negatively detected the positive predictive value shows proportion of optic disk pixels which correctly detected.

$$Accuracy = \frac{(TP+TN)}{(TP+FN+TN+FP)} x100 \quad (5.13) \qquad Sensitivity(\%) = \frac{TP}{TP+FN} x100 \quad (5.14)$$

$$Specificity(\%) = \frac{TN}{TN + FP} x100 \qquad (5.15) \qquad PPV(\%) = \frac{TP}{TP + FP} x100 \qquad (5.16)$$

After all the sixty retinal images were processed, they were compared with the hand-drawn ground-truth images marked by ophthalmologist and the result will be discussed in the next section.

5.4 Experimental Results

Two set of images were used in this experiment. The first set of thirty images was images from ROP infants while the second set was a set of images with diabetic retinopathy. The result of detection for the fist set is demonstrated in Table 5.2 and 5.3 respectively.

Table 5.2 The examples of accuracy, sensitivity and specificity result in retinal image with ROP condition

Image	TP	TN	FP	FN	Accuracy	Se(%)	Sp(%)	PPV(%)
A11g	1262	305678	246	14	99.9	98.9	99.9	83.7
A12g	1405	305590	204	1	99.9	99.9	99.9	87.3
A13g	1344	305627	202	27	99.9	98.0	99.9	86.9
A17g	1562	305412	132	94	99.9	94.3	100.0	92.2
A19g	1627	305337	192	44	99.9	97.4	99.9	89.4
A5g	1400	305484	315	1	99.9	99.9	99.9	81.6
A6g	1595	305461	115	29	100.0	98.2	100.0	93.3
A7g	1383	305575	169	73	99.9	95.0	99.9	89.1
A8g	1461	305554	168	17	99.9	98.8	99.9	89.7
A9g	1412	305570	165	53	99.9	96.4	99.9	89.5
B3g	2107	304678	291	124	99.9	94.4	99.9	87.9
C10g	1371	305531	162	136	99.9	91.0	99.9	89.4
C11g	1266	305774	156	4	99.9	99.7	99.9	89.0
C12g	1320	305716	164	0	99.9	100.0	99.9	88.9
C13g	1398	305617	116	69	99.9	95.3	100.0	92.3
C2g	1396	305508	270	26	99.9	98.2	99.9	83.8
C6g	1417	305550	181	52	99.9	96.5	99.9	88.7
C7g	1351	305685	131	33	99.9	97.6	100.0	91.2
C8g	1328	305721	142	9	100.0	99.3	100.0	90.3
C9g	1366	305610	85	139	99.9	90.8	100.0	94.1
D10g	1685	305311	159	45	99.9	97.4	99.9	91.4
D11g	1831	305151	114	104	99.9	94.6	100.0	94.1
D14g	1799	305263	56	82	100.0	95.6	100.0	97.0
D18g	1752	305115	109	224	99.9	88.7	100.0	94.1
D19g	1773	305155	82	190	99.9	90.3	100.0	95.6
D2g	1318	305673	180	29	99.9	97.8	99.9	88.0
D4g	1421	305536	161	82	99.9	94.5	99.9	89.8
D6g	1489	305533	133	45	99.9	97.1	100.0	91.8
D7g	1402	305613	139	46	99.9	96.8	100.0	91.0
D8g	1479	305569	135	17	100.0	98.9	100.0	91.6
Over all					**99.9**	**96.4**	**99.9**	**90.1**

Table 5.3 The examples of accuracy, sensitivity and specificity result in retinal images with diabetic retinopathy.

Image	TP	TN	FP	FN	Accuracy	Se(%)	Sp(%)	PPV(%)
10E	3252	303446	502	0	99.8	100.0	99.8	86.6
11CE	3316	303493	381	10	99.9	99.7	99.9	89.7
12EH	3828	302769	603	0	99.8	100.0	99.8	86.4
18E	3988	296505	3446	166	98.8	96.0	98.9	53.6
19E	3357	303250	524	69	99.8	98.0	99.8	86.5
1ACEH	7070	299588	518	24	99.8	99.7	99.8	93.2
22CH	4497	302073	628	2	99.8	100.0	99.8	87.7
23E	4494	302216	451	39	99.8	99.1	99.9	90.9
25E	3131	303499	539	31	99.8	99.0	99.8	85.3
26E	3155	302411	1622	12	99.5	99.6	99.5	66.0
29EH	4466	301838	626	270	99.7	94.3	99.8	87.7
2ACEH	6369	299944	887	0	99.7	100.0	99.7	87.8
33E	4448	301891	861	0	99.7	100.0	99.7	83.8
34E	4554	302173	472	1	99.8	100.0	99.8	90.6
35AEH	6950	299522	723	5	99.8	99.9	99.8	90.6
36ACE	6494	299944	762	0	99.8	100.0	99.7	89.5
38E	4983	301076	1136	5	99.6	99.9	99.6	81.4
39E	4582	301853	765	0	99.8	100.0	99.7	85.7
3E	3085	303475	585	55	99.8	98.2	99.8	84.1
45E	4464	302027	706	3	99.8	99.9	99.8	86.3
46E	5433	295156	3849	0	98.7	100.0	98.7	58.5
49E	4123	300366	2708	3	99.1	99.9	99.1	60.4
53E	4399	301892	907	2	99.7	100.0	99.7	82.9
59sn	5290	298922	1843	20	99.4	99.6	99.4	74.2
5EH	4220	302267	696	17	99.8	99.6	99.8	85.8
67CE	4889	301619	663	29	99.8	99.4	99.8	88.1
6EH	4279	302420	487	14	99.8	99.7	99.8	89.8
71E	4765	301839	596	0	99.8	100.0	99.8	88.9
7E	4154	302401	642	3	99.8	99.9	99.8	86.6
8H	4234	302085	875	6	99.7	99.9	99.7	82.9
Over all					**99.7**	**99.4**	**99.7**	**83.1**

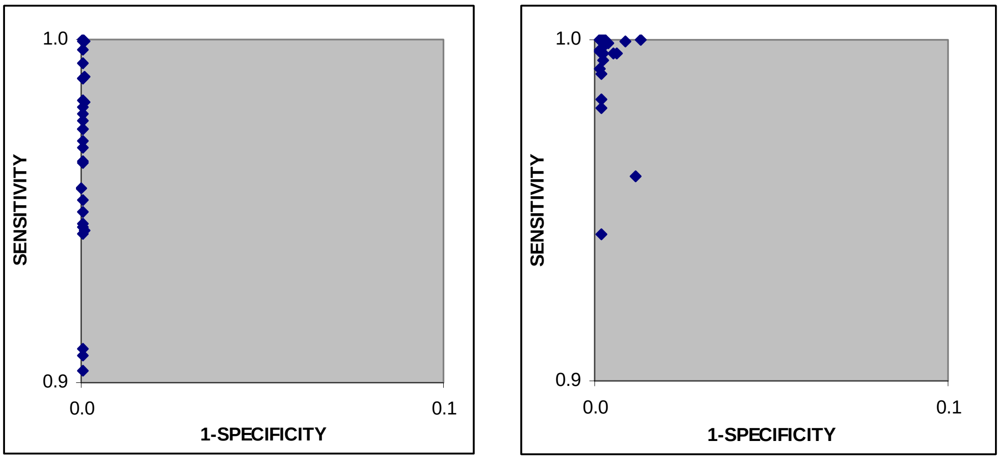

(a) (b)

Figure 5.10 (a) The sensitivity and specificity result in retinal image with ROP condition (b) The sensitivity and specificity result in retinal images with diabetic retinopathy

For optic disk in ROP infant, the overall accuracy, sensitivity, specificity and PPV value achieved by this method are 99.9%, 96.4%, 99.9% and 90.1% respectively (Figure 5.10(a)). The overall accuracy, sensitivity, specificity and PPV value for optic disk detection in diabetic retinopathy retinal image are 99.7%, 99.4%, 99.7% and 83.1% respectively (Figure 5.10(b)). All of sixty optic disks of low-contrast images were identified by this proposed algorithm.

5.5. Conclusion and Discussion

We have presented an automatic method for Optic Disk detection based on Mathematical Morphology. Histogram enhancement and filtering techniques were used to enhance image quality in red channel. Canny edge detection was applied to detect edge line in the previous result. Morphological Closing was first applied. Mathematical morphology (Dilation and Erosion) and connected component labeling were then applied to extract the optic disk from the retinal image. The detection results were validated against clinicians' hand-drawn ground truth. The result of images with ROP (infant retina) was quite successful with accuracy of 99.9% while the accuracy of the result from adult retinal images is 99.7%. This method is able to identify correct position of all optic disk in ROP Infant as well as in adult's retinal image with diabetic retinopathy. From this experiment, the total processing time of optic disk detection for each image is 15 seconds with 3 GHz Pentium 4 machine. Visible advantages of this algorithm are that it works pretty well on low-contrast retinal image with ROP with fast computation and quite reliable. This algorithm could facilitate clinicians to analyze the area surrounding the optic nerve.

Chapter 6

Conclusions

This chapter summarizes all research works in this dissertation. The key contributions are listed and some recommendations for future research are also discussed.

6.1 Research Summary

This thesis presented algorithms of automatic detection of optic disk from low-contrast fundus images of ROP Infant. All techniques are implemented in 3 GHz Pentium 4 machine. The first technique is based on Circular Hough Transform and Canny Edge Detection to detect the optic disk. The Circular Hough Transform histogram is reduced from 3D to 2D then in the calculation process, a value in particular point in Hough space is accumulated. After that, it was thresholded to leave only points with high probability of being the centers. The OD position was considered correctly detected if the pixels in the detected image present in the clinician's hand-drawn ground truth. In the finally, we find the best circle to fit the optic disk. The accuracy result of this method is achieved 81.7% from a data set of fifty infant fundus images. The time consuming for 2D Circular Hough Transform technique is 12 seconds for each image. The second method is achieved using PCA and deformable contour model with gradient vector flow as an external force. The first snake is placed at a location very close to the center of the optic disk approximated by PCA based model. The accuracy result is quite successful with 85.34% from a data set of fifty infant fundus images and the rate of convergence for each image is 10 seconds. One visible advantage of this method is that the optic disks are detected even though the boundary of the optic disk is not continuous or blurred. The last method, we use mathematical morphology to detect the optic disk. This method is based on mathematical morphology. We use many techniques to detect the region of optic disk, Histogram equalization and average filtering techniques were used to enhance Red band of the original low-contrast retinal image. The blood vessel was eliminated from the retinal image using the morphology closing. Optic disk localization is then achieved using optimized mathematical morphology and connected labeling. The result of thirty infant's retinal images with ROP condition and thirty images from diabetic retinopathy patients were validated with experts' hand-drawn ground truth. The result is quite successful with the accuracy of 99.9 % for retinal images with ROP and 99.7% for diabetic retinopathy retinal images. The time consuming in morphology technique is 15 seconds for each image. This method is able to identify correct position of all optic disk in ROP Infant as well as in adult's retinal image with diabetic retinopathy. Visible advantages of this algorithm are that it works pretty well on low-contrast retinal image with ROP with fast computation and quite reliable. This algorithm could facilitate clinicians to analyze the area surrounding the optic nerve. For the verification results were compared and validated with experts' hand-drawn ground truth.

In all three algorithms, they work pretty well in low-contrast retinal image with ROP. All three prototypes have been implemented in MATLAB 7.0.4(R14) on a 3.00 GHz PC under Windows XP.

6.2 Key Contributions of the Research

1. To find an efficiency algorithm to detect the optic disk in ROP Infant retinal image
2. Implement an automatic program to detect the optic disk in ROP Infant
3. To help the clinician to diagnose the ROP in the earlier stage that can prevent the infant blindness
4. To protect Thai infant from blindness with ROP

6.3 Future Study

As the future study of detection of optic disk in ROP Infant, we try develop this demo in the package of application software because all of algorithms were implemented in MATLAB. That is not convenient for clinician to handle, if we develop in application software which easy to use, it will be the efficiency tool for medical doctor to diagnosis the ROP disease in the rural area in Thailand.

References

Acharya, T. and Ray, A.K. 2005. Image Processing Principles and Applications. Wiley, New Jersey, U.S.A.

Akita, K. and Kuga, H., 1982. A computer method of understanding ocular fundus images. Pattern Recognition., 5(6):431-443

Awcock, G.W. and Thomas, R., 1996. Applied Image Processing, McGraw Hill International Editions.

Chanwimaluang, T. and Fan, G., 2003. An efficient algorithm for extraction of anatomical structures in retinal images. IEEE International Conference on Image Processing, Barcelona, Spain, September, 2003, p. 1,093-1,096.

Chrástek, R., Skokan, M., Kubecka, L., Wolf, M., Donath, K., Jan, J., Michelson, G. and Niemann, H., 2004. Multimodal Retinal Image Registration for Optic Disk Segmentation. Methods of Information in Medicine. 43:336-342.

Corona, E., Mitra, S., Wilson, M., Krile, T., Kwon, Y.H. and Soliz, P., 2002. Digital stereo image analyzer for generating automated 3-D measures of optic disc deformation in glaucoma. IEEE Trans. Med. Imaging. 21:1,244-1,253.

Costaridou, L., 2005. Medical Image Analysis Methods. CRC Press, New York, p. 438-440.

Cox, M.J. and Wood, I.C.J., 1991. Computer assisted optic nerve head assessment. Ophthal. Physiol. Opt., 11:27-35.

Davatzikos, C.A. and Prince, J. L., 1995. An active contour model for mapping the cortex. IEEE Transaction. Medical Imaging., 14(1):65–80.

Foracchia, M., Grisan, E. and Ruggeri, A., 2004. Detection of optic disc in retinal Images by means of a geometrical model of vessel structure. IEEE Transactions on Medical Imaging, 23(10):1,189-1,195.

Gong, S., McKenna S.J. and Psarrou, A., 2000. Dynamic Vision From Images to Face Recognition. Imperial College Press, London, p. 297-300.

Gonzalez, R.C. and Woods, R.E. 2002. Digital Image Processing 2nd Edition. Prentice Hall, New Jersey, U.S.A.

Grimson, W. E. L., Ettinger, G. J., Kapur, T., Leventon, M. E., Wells, W. M. and Kikinis, R., 1997. Utilizing segmented MRI data in image-guided surgery. Int'l J. Patt. Recog. Artificial Intell., 11(8):1,367–1,397.

Jelinek, H.F., Depardieu, C., Lucas, C., Cornforth, D., Huang, W. and Cree, M.J., 2005. Towards vessel characterisation in the vicinity of the optic disk in digital retinal images. McCane (ed.), Proceedings of the Image and Vision Computing Conference, New Zealand 2005, University of Otago.

Kass, M., Witkin, A. and Terzopoulus, D., 1987. Snakes Active Contour Models, Proceedings of First International Conference on Computer Vision, London, 1987, p. 259-269

Kavitha, D. and Shenbaga Devi, S., 2005. Automatic Detection of Optic Disc and Exudates in Retinal Images. IEEE Int. Conf. On Intelligent Sensing and Information. Processing (ICISIP). Jan, 2005, p. 501-506.

Kong, H. J., Kim, S.K., Seo, J.M., Park, K. H.,Chung, H., Park,K.S. and Kim, H.C., 2004. Three Dimensional Reconstruction of Conventional Stereo Optic Disc Image. Annual International Conference of the IEEE EMBS; September 1-5, 2004; p. 1,229-1,232.

Lalonde, M., Beaulieu, M. and Gagnon, L., 2001. Fast and robust optic disk detection using pyramidal decomposition and Hausdorff-based template matching. IEEE Transactions on Medical Imaging, 20(11):1,193-1,200.

Lee, S. 1991. Visual Monitoring of Glaucoma, Ph.d. Robotics Research Group, Department of Engineering Sceince, University of Oxford, Available on micro-fiche.

Li, H. and Chutatape, O., 2001. Automatic location of optic disk in retinal Images. Proceedings of IEEE-ICIP; October 7-10, 2001; Thessaloniki, Greece, p. 837–840.

Li, H. and Chutatape, O., 2003. Boundary detection of optic disk by a modified ASM Method. Pattern Recognition. 36:2,093-2,104

McNamara, J.A., Connolly, B.P., 1999. Retinopathy of prematurity. In: Regillo, C.D., Brown, C.G., Flynn, H.W. (Eds.), Vitreoretinal Disease: The Essentials. Thieme Medical Publishers, New York, p. 177-192.

Mendels, F., Heneghan, C. and Thiran, J.P., 1999. Identification of the optic disc boundary in retinal images using active contours. Proceedings of the IMVIP Conference, 1999, p. 103-115.

Moris, D.T., Cox, M.J. and Wood, I.C.J., 1993. Automated Extraction of The Optic Nerve Head Rim. American Association of Optometrists Annual Conference; December 1993; Boston, p. 11-22

Niemeijer, M., Abramoff, M.D., Van Ginneken, B., 2007. Segmentation of the optic disc, Macula and vascular arch in fundus photographs. IEEE Transactions on Medical Imaging. 26:116-127.

Osareh, A., Mirmehdi, M., Thomas, B. and Markham, R., 2002. Colour Morphology and Snakes for Optic Disc Localisation. The 6th Medical Image Understanding and Analysis Conference, July 2002.

Palmer, E.A., Flynn, J.T., Hardy, R.J., Phelps, D.L., Phillips, C.L., and Schaffer, D.B., 1991. Incidence and early course of retinopathy of prematurity. Ophthalmology 98:1628–1640.

Sinthanayothin, C., Boyce, J.F., Cook, H.L. and Williamson, T.H. 1999. Automated localization of the optic disc, fovea, and retinal blood vessels from digital color fundus images. Br J. Ophthalmol., 83(8):902-910.

Terzopoulos, D., 1987. On matching deformable models to images. Technical Report 60, Schlumberger Palo Alto research, 1986. Reprinted in Topical Meeting on Machine Vision, Technical Digest Series, 12:160-167.

Tobin, K.W., Chaum, E., Govindasamy, V.P., Karnowski, T.P. and Sezer, O., 2006. Characterization of the optic disk in retinal imagery using a probabilistic approach. Proc. SPIE, p. 6,144.

Williams, D.J. and Shah, M., 1992. A Fast Algorithm of Active Contours and Curvature Estimation, CVGIP: Image Understanding, 55(1), January 1992, p. 14-26.

Xu, C. and Prince, J. L., 1997. Gradient Vector Flow: A New External Force for Snakes. Proceedings of IEEE Conf. on Comp. Vis. Patt. Recog. (CVPR); June 1997; Los Alamitos, p. 71.

Xu, C. and Prince, J. L., 1998. Snakes, shapes and gradient vector flow. IEEE Trans Imag.Proc., 7(3):359–369.

Zijdenbos, A. P. and Dawant, B. M. (1994). Brain segmentation and white matter lesion detection in MR images. Critical Reviews in Biomedical Engineering, 22(5-6):401–465.

Appendix A

List of Publications

A.1 National Journal

Thongnuch, V. and Uyyanonvara, B. Automatic Optic Disk Detection from Low Contrast Retinal Images of ROP Infant Using GVF Snake, Suranaree Journal of Science and Technology 14(3):215-226.

A.2 International Conference

Thongnuch, V. and Uyyanonvara, B. Automatic Detection of Optic Disk from Fundus Images of ROP Infant Using 2D Circular Hough Transform, in Proceedings of ISBME 2006, Bangkok, Thailand, 2006, p. 328-330.